Supplementary Text

Strategizing intratumoral injection of the nanoparticles

T1-weighted MRI (using gadolinium (Gd)-based contrast agent) was used to localize orthotopically-implanted tumors and calculate their volume in mouse brains (Supplementary Fig. 21). Nanoparticle injection timelines were chosen based on the tumor size, determined by bioluminescence imaging (BLI) and MRI (Fig. 1D and E). Micro-injection was used for MRI-guided delivery of the nanoparticles (hydrodynamic size ~140 nm, dosage ~1 μL, 0.5 nM) into the tumors. Stereotactic intratumoral injection enabled precise delivery of the required dosage of the nanoparticles to the tumors in any region of the interest in the brain. Therefore, we did not encounter any nanoparticle delivery issue in this approach. Also, our nanoparticles were accumulated in the brain tumors over the entire treatment without getting transferred to other organs. Also, we did not see traces of nanoparticles in adjacent normal brain tissues, as verified by fluorescent microscopy of the brain tissues at the end of the survival period (Supplementary Fig. 7, also confirmed by ICP elemental analysis of the tissues). This was a significant advantage compared to conventional intravenous administration approaches, which are based on injection of much higher dosages (*e.g.*, 100-1000x higher dosages) that mostly (~98%) accumulate in liver and spleen. The micro-dosages of the nanoparticles we injected into tumors were sufficient for photothermal treatment.

Photothermal response of the nanoparticles

Continuous irradiation of the nanostars for photothemrmal therapy often results in their morphological transition to nanospheres, which have less photothermal heating efficacy [1]. This is mainly attributed to diffusion of gold atoms at higher temperatures to make spherical particles with lower surface energy, which is a thermodynamically preferred state. This phenomenon results in a rapid shift in light absorption peak of these nanoparticles, and decreases their photothermal response rate and therefore their therapeutic effect after a short irradiation time. Our gold nanostar particles were designed for enhanced surface plasmon and photothermal response when irradiated with various forms of NIR tissue penetrating light. These nanoparticles could feasibly respond to a wide range of pulsed or continuous optical signals (*i.e.*, 800-1050 nm wavelengths, and 10-70

mW optical power) delivered from our wirelessly-powered NIR-emitting devices that were subcutaneously implanted on the skull. Among different morphologies and aspect ratios of the nanostars, we chose one which could maintain morphological stability for sufficient heating during a long-term pulsed irradiation (*i.e.*, after long-term, 15 min/day for 15 days, duty-cycled irradiation at 4 V, Supplementary Fig. 8), because our subcutaneously implanted NIR-emitting devices showed maximum wireless signal transfer efficacy and safety in pulsed irradiation mode. Thermal analysis of the irradiated nanostars also confirmed their consistent photothermal response at the end of this long-term 15-day pulsed irradiation, due to their morphological stability.

Three energy transfer kinetics are involved in photothermal response of these nanoparticles, when they are under NIR irradiation: (*i*) electron-electron scattering in a single particle to relax from a non-Fermi to Fermi electron distribution (<100 fs); (*ii*) electron-phonon scattering for heat generation in a single particle (1-10 ps); and (*iii*) phonon-phonon scattering to transfer heat from a nanoparticle to its environment (~100 ps) [2]. Even though the surface plasmon and photothermal response of the nanoparticles are ultrafast electronic phenomena, we found that macroscopic photothermal response, and therefore, tumor treatment efficiency of our nanoparticles, did not change when a pulsed (duty-cycled) irradiation was used to activate them. This characteristic of our nanoparticles enabled us to tune the wireless signal transfer parameters and frequency of the irradiation pulses, to build a safe wireless activation setup to induce sufficient photothermal response in the brain.

Targeted heating of the tumors

Nanoparticles only diffused into tumor tissues (Fig. 1H-J and Supplementary Figs. 3, 4, and 7) because of their enhanced permeation and retention in tumor and therefore photothermal effects were localized at the tumor site (Supplementary Fig. 9). Photothermal heating is highly dependent on nanoparticles concentration, and optical power reaching to them. Even if some negligible amount of nanoparticles diffused into adjacent normal brain tissues, they were not expected to generate heat during our photothermal treatments because (*i*) a sufficient concentration of the nanoparticles was required to generate observable heat (or elevated temperatures) at the tissue scale and (*ii*) the 810- and 940-nm lights emitted from our devices were targeted to tumor area for highest photothermal treatment efficiency and therefore minimal percentage of the emitted photons

were delivered to surrounding normal brains, which further decreased the probability of heating other parts of the brain tissues. As a result of this tumor targeted heating, we did not observe any behavioral change or interruption in normal activities of the mice during and after treatment sessions. Therefore, unlike the state-of-the-art photothermal therapy methods which are limited to a single-session intraoperative treatment, our wirelessly powered opto-electrical interface, enabled continuous and long-term irradiation of the tumors over the entire survival period, without any additional surgery, or need of anesthetic or analgesic agents to expose the tumors for optical irradiation and photothermal treatment.

Modeling light penetration in mouse brain

First, we used diffusion theory to estimate the light transport in brain based on the attenuation length of light in brain tissue at different wavelengths and a model reported before [3]. This model accounts for both light absorption and scattering in the mouse brain and suggests that the ratio of the optical power at a depth z from the point source located at the origin, decays exponentially according to

$$Ratio(z) = e^{-\frac{z}{\ell}} \quad \text{(S1)}$$

where ℓ is the attenuation length, a constant that is determined by tissue type and wavelength. We used this equation and attenuation lengths (as well as other brain tissue optical properties) obtained from this report [3] to assess attenuation patterns at different wavelengths and the results are shown in Supplementary Fig. 10. As a simplified model, we first calculated the light intensity in the brain, based on Beer-Lambert law (assuming LEDs as planar light sources), using radiation patterns of our LEDs provided by the manufacturer, and the tissue attenuation equation described above. We repeated the same calculations for other wavelengths for comparison. The transmittance patterns (*i.e.*, $I_{(z)}/I_0$, where I_0 is the light intensity at the LED surface) in the brain for LEDs emitting different wavelengths are shown in Supplementary Figs. 11A-E. Finally, we employed Monte Carlo simulation (using the MonteCarloLight MATLAB script provided in a previously published report [4]) to determine the light penetration pattern in the brain considering LEDs as point light sources and the results are shown in Supplementary Figs. 11F-K for comparison. Here, the radius

of the light-emitting area of the LED (~ 0.8 mm) was considered as the dimeter of the point source, with a numerical aperture of ~ 0.236, approximated using a beam angle of 10° for the LED in a brain medium with refraction index of 1.36 [4].

LED electrical to optical efficiency characterization

The applied DC voltage to each LED was swept manually from voltages below the forward voltage of the LED to a voltage level generating maximum allowable current through the LED, I_{max}, using the DC power supply. LED efficiency was defined as $\eta(\%) = \frac{P_{optical}}{P_{electrical}} \times 100$, where $P_{electrical} = IV$ (V is the applied voltage and I is the current through the LED). The power supply was set to around the voltage level which yielded at least 25 mW of optical power and the applied voltage was fine-tuned to result in at least 3 ºC increase in the nanoparticles' temperature. Required power levels were recorded for further calculations.

Selection of the LEDs

To fabricate the NIR-emitting devices, we first selected several commercially available NIR LEDs based on their size, radiation wavelength, emission power, and beam shape. Then, we characterized their electrical to optical efficiency for sufficient heating of the nanoparticles (*i.e.*, ΔT~ 3-5 ºC, due to their surface plasmon resonance), as well as self-heating of the LEDs. Two LEDs were chosen for our studies and are referred to as 810-nm and 940-nm LEDs in the manuscript.

Duty-cycle estimation of the back-to-back LED topology

The voltage and current waveforms of the single and back-to-back LED topologies are shown in Figs. 2G-H. We assume the LEDs do not conduct ($i_D = 0$) when the voltage across them is less than the forward voltage (V_F). For the single LED topology (Fig. 2G and Supplementary Fig. 16A), when the input voltage (V_{in}) is less than V_F ($V_{in} < V_F$), the LED is off, while the output voltage

follows V_{in}. As $V_{in} > V_F$, $V_{out} = V_F$ and remains at this level and the current through the LED during $\tau_1 < t < \tau_2$ can be written as:

$$i_{LED} = \frac{V_{in} - V_F}{R_s} = \frac{V_0 \sin(2\pi f_0 t) - V_F}{R_s} \quad \text{(S2)}$$

in which V_0 and f_0 are the amplitude and frequency of input voltage (V_{in}). Note that:

$$\tau_1 = \frac{1}{2\pi f_0} \sin^{-1}\left(\frac{V_F}{V_0}\right) \quad \text{(S3)}$$

and

$$\tau_2 = \frac{1}{2\pi f_0} \left[\pi - \sin^{-1}\left(\frac{V_F}{V_0}\right)\right] \quad \text{(S4)}$$

Therefore, average power delivered to the LED can be written as:

$$P_{avg} = \frac{1}{T} \int_{\tau_1}^{\tau_2} i_{LED} V_F dt \quad \text{(S5)}$$

and it follows that:

$$P_{avg} = \frac{V_0 V_F}{\pi R_s} \sqrt{1 - \left(\frac{V_F}{V_0}\right)^2} - \frac{V_F^2}{R_s} \left[\frac{1}{2} - \frac{\sin^{-1}\left(\frac{V_F}{V_0}\right)}{\pi}\right] \quad \text{(S6)}$$

We define the duty cycle as:

$$d = \frac{P_{avg}}{P_{dc}} \quad \text{(S7)}$$

where:

$$P_{dc} = V_F \frac{V_0 - V_F}{R_s} \quad \text{(S8)}$$

However, in back-to-back design (Fig. 2H and Supplementary Fig. 16B), each diode is turned on during one half cycle, and therefore, the power delivered to the LEDs is twice the value calculated in Eq. S6. This is because:

$$P_{avg} = \frac{1}{T} \left[\int_{\tau_1}^{\tau_2} i_{LED} V_F dt + \int_{\tau_3}^{\tau_4} (-i_{LED})(-V_F) dt\right] \quad \text{(S9)}$$

where:

$$\tau_3 = \frac{1}{2\pi f_0} \left[\pi + \sin^{-1}\left(\frac{V_F}{V_0}\right)\right] \quad \text{(S10)}$$

and

$$\tau_4 = \frac{1}{2\pi f_0} \left[2\pi - \sin^{-1}\left(\frac{V_F}{V_0}\right)\right] \quad \text{(S11)}$$

and τ_1 and τ_2 are given by Eqs. (S3) & (S4). For the back-to-back design, LEDs were alternately turned on with a maximum duty-cycle of 31.8%, mitigating LED heating, while providing over-voltage protection to the other LED during the negative half-cycle.

Comparison of the conventional RF-to-DC converter efficiency with the back-to-back design

Our circuit simulation (Supplementary Fig. 17) suggested power conversion efficiencies (PCE) of about 32.7% and 42% for the topologies shown in Figs. 2G and 2H, respectively, at the same electrical output power level, which was required to trigger nanoparticles photothermal response. Increasing the number of RF-to-DC converter stages in the conventional design boosts [5] the output power for more photothermal effect, but at the cost of lower PCE (Supplementary Fig. 17). CTS05S30 Schottky diodes (Toshiba, Japan) were used in the simulation of the RF-to-DC converter.

Definition of the various device efficiency parameters

η_{MN} is the overall efficiency of the matching network defined as the ratio of the output power of the matching network to P_{avs} (the available power from the antenna, $P_{avs} = 0.5\ P_{in}$, where P_{in} is the incident power at the antenna), which can be expressed as $\frac{P_{out,MN}}{P_{avs}} = \eta_{MN} = (1 - |S_{11}|^2).IL.$ Here, $P_{out,MN}$ is the power provided by the matching network (applied to the LEDs) and IL is the insertion loss of the matching network and is related to the quality factor of the matching elements. For our implementation, since there is no rectifier (Fig. 2H), $P_{out,MN}$ is the power, which is directly delivered to the LEDs, *i.e.*, $P_L = P_{out,MN}$.

η_{rec} refers to the electrical efficiency of the rectifier, defined as $\eta_{rec} = \frac{P_L}{P_{out,MN}}$, where $P_{out,MN}$ is the power that the matching network can deliver to the rectifier, and P_L is the power that the rectifier delivers to the LEDs. η_{rec} is independent of η_{MN}.

Also, the PCE or power conversion efficiency is defined for electrical parameters as the ratio of the power delivered to the load (LEDs) and the input power to the antenna, *i.e.*, $PCE = P_{LED}/P_{in}$.

The values of these parameters are listed in the following table:

Parameter	Value
η_{MN}	93.7%*
η_{rec}	69.6%
PCE (Back-to-back LED)	41%
PCE (Conventional)	32.7%**

*Assuming S_{11} = -20 dB
** For single-stage (N = 1), S_{11} = -20 dB

Back-to-back LED RF characterization and matching for maximum power delivery and sufficient photothermal efficacy

To achieve optimal power transfer to nanoparticles in the brain, the NIR-emitting LEDs (Supplementary Fig. 12A) were matched to the antenna impedance at NFC frequency. First, we used large-signal S-parameter (LSSP) simulations (verified with measurement) to match the impedance of the BB LEDs (for both 810-nm and 940-nm prototypes) to that of the antenna at the nominal input power level (19 dBm) at 13.56 MHz (Fig. 3A-B and Supplementary Fig. 19A). At the frequency of interest, the antenna on the device showed an inductive behavior with an impedance of $\mathrm{Z_{ant}} = 9.2 + \mathrm{j}239$ (Fig. 3B).

The measured (and simulated) input impedance values at the power levels of interest for the 810- and 940-nm LEDs were $\mathrm{Z_{in}} \approx 21.5 - \mathrm{j}10.5$ and $\mathrm{Z_{in}} \approx 23.7 - \mathrm{j}8.4$, respectively, suggesting a capacitive impedance. A simulation model was also developed based on the measured data at 13.56 MHz and the input power range of 14-20 dBm using harmonic balance simulation in ADS simulator for both LED designs. We modified a commercially available RFID transponder at 13.56 MHz (dimensions: 8.3 mm × 8.3 mm × 0.7 mm, LXMSAPHA17-176, Murata Electronics, Japan) comprising a radiofrequency identification (RFID) chip and an integrated antenna (copper traces) on a flexible substrate to make our NIR-emitting devices by removing the RFID chip and carving out a rectangular area at the center to place the LEDs (Fig. 2B and Supplementary Fig. 14). At the frequency of interest, the antenna exhibited an inductive behavior with an impedance of $\mathrm{Z_{ant}} = 9.2 + \mathrm{j}239$ (red triangles shown with arrows in Fig. 3A and Supplementary Fig. 19A). High-Q capacitors were used for impedance matching to minimize insertion loss (Fig. 3C and Supplementary Fig. 19B).

Specific absorption rate (SAR) simulation

1-g SAR is defined as SAR averaged over 1 gram of tissue with the shape of a cube per FCC [6]. Our SAR simulations resulted in 1-g SAR values of 1.37 and 56.4 W/kg at 13.56 and 915 MHz, respectively, (PA output power of 38 dBm). The absorption at 915 MHz was ~16 dB more than the absorption for a mouse in 13.56 MHz field. Such a significantly higher absorption rate is attributed to dimensions of the mouse (~ 3 cm × 4 cm × 11 cm, weight 22-28 g) that are typically about a quarter of the wavelength of the incident waves at 915 MHz. This geometrical correlation resulted in partial resonance and therefore, more effective coupling between incoming electromagnetic waves and tissues. This coupling enhanced transfer of the energy to the tissues and increased the mouse body temperature at 915 MHz. Since the wavelength at 13.56 MHz is around 70 times longer than the 915 MHz waves, coupling of the waves to the mouse body was significantly weaker (*i.e.*, almost 2.4% of the absorption at 915 MHz for the same power level), and yet, we could achieve sufficient photothermal effect from the nanoparticles in the tumor. Therefore, we chose 13.56 MHz frequency as a much safer option for our high-power wireless approach.

Thermal analysis of the devices

810-nm and 940-nm devices reached their maximum temperatures after ~ 1, 2, and 4 min, when tested at low, medium, and high power levels, respectively at h = 0 cm, where we expected the highest power transfer and maximum heating. LEDs and their pads were relatively warmer compared to other parts of the device. Warmest spots on the 810-nm and 940-nm devices were {28.8, 29.5, and 31 °C} and {30.3, 40.9, and 54.6 °C}, respectively, when the highest power parameters were applied. Note that these values were local maximum (spatial peak) and the average temperatures of the devices were significantly lower in real *in vivo* conditions. For example, variations of the mouse body temperature around an implanted 940-nm device, running at the highest power level, showed that maximum temperature variation (ΔT_{max}) observed around the device was ~1.8 ºC (Supplementary Fig. 34).

Designing the photothermal therapy protocol

The near-infrared photons generated by the LEDs and their interactions with nanoparticles embedded in the tumors define the therapeutic interface between our wirelessly-powered devices and brain tumors. Therefore, light-emitting power of the implanted devices and NIR absorption efficacy of our nanoparticles were key factors for effective treatment in our approach. The power transfer setup, coils geometry, and power levels were tuned to generate sufficient optical power from the devices (*i.e.*, 25-50 mW) at 1 cm < h < 5 cm, where h is the distance between the implanted device and the TX coil. We chose this height range since our statistically confirmed observations showed that the mouse head was consistently within this selected measurement distance during free-behaving photothermal therapy sessions. The link efficiency and the tissue loss were estimated from electromagnetic simulation to determine required output power levels (~32 dBm at the TX antenna corresponding to ~ –10 dBm at the PA input).

The treatment protocol (timeline, duration, power levels, nanoparticles concentration, tumor implantation depth, and starting point of the treatments) were chosen based on a combination of our overall experimental observations and previously reported studies [7,8]. The continuous photothermal therapy (15 min/day) and multiple powering were chosen to ensure sufficient heating of the tumors with minimal thermal effects on surrounding brain tissues and we repeated photothermal therapy sessions for 15 days to enhance the therapeutic effect. We saw shorter survival in mice that received shorter daily treatments (5 and 10 min/day) or treated during shorter periods (5 and 10 days). Our statistical observations suggested that freely-behaving mice suffering from brain tumors often stay in positions which places the top of the head (location of the implanted device) at ~3 cm from the bottom of the therapeutic chamber (TX coil). As such, for an approximate estimation of the best *in vivo* experimental parameters, we placed an *ex vivo* sample of the nanoparticles at this height and measured their photothermal heating effect in response to irradiation with different power levels used to activate the 810- and 940-nm devices. Based on the literature, we also considered ΔT values of ~3-5 °C, as the effective and safe range of heating for brain tumor photothermal therapy [8]. Additionally, these two devices had different electrical-to-optical power transformation efficiencies, that could result in different photothermal heating efficacies, if we used exactly similar powering parameters for both of them. Therefore, we adjusted the power levels and their duration for each device to generate approximately similar amounts of heat in the tumors during the 15 min treatment cycles, and this similarity helped for better

comparison of the survival results in different groups of mice. It also helped to prevent heating of the adjacent normal brain tissues, and enabled us to control the device temperature. For 810 nm devices, we chose 7 min at -9 dB (ΔT~ 3 °C), 5 min at -6 dB (ΔT~ 4 °C), and 3 min at -3 dB (ΔT~ 5 °C), and for 940 nm devices, we chose 13 min at -10 dB (ΔT~ 3.5 °C), 1 min at -7 dB (ΔT~ 4.5 °C), and 1 min at -4 dB (ΔT~ 5 °C). Choosing these parameters enabled us to generate approximately the same amount of heat in tumors in animals implanted with different devices. Multiple powering also helped to compensate for possible power variations due to varying position of the mouse head during the treatments.

Approximate estimation of clinical benefits from survival data in mice studies:

Generally, comparing the average lifespans of each species and extrapolating a survival benefit in mice (days/weeks) to a human (weeks/months/years) is not accurate. This is because the survival is highly dependent on the model system used for studies. For each model system, if X number of Y cells get injected into a mouse brain of age Z weeks, then (on average), the median survival in that specific model system is W weeks. Also, the same [or scaled] dose of radiation or chemo-drugs are not given to mice models compared to humans, and surgeries are not used in mice (which is often used in humans). Additionally, effects of the different microbiomes, metabolisms, diet, immune systems (or lack thereof in nude mice) should be carefully considered for any comparison between species.

Considering all of these variables and neglecting all the biological factors, a very simplistic way of comparing the survival outcomes can be looking at the ratio of survival difference of the intervention (treated - untreated) divided by the average lifespan of that species. The median overall survival of patients with GBM who get standard surgery, radiation (X-ray therapy or XRT), and temozolomide (TMZ) is ~16 months [9]. Therefore, for humans with GBM, this ratio would be (16 months of survival benefit with surgery/XRT/TMZ - 6 months of survival benefit without surgery/XRT/TMZ [10]) / 80 year life expectancy for Europeans/Americans = 0.0104.

We did the same calculation for the mice based on the data presented in Fig. 4F (in which median survival in treatment 3 was 9.5 days and median survival in control 3 was 3.5 days):

(9.5 days - 3.5 days) / 1,060 (days lifespan of nude mice [11]) = 0.0057

Therefore, based on this rough analysis, with photothermal therapy alone (not including standard surgery, radiation, and chemotherapy), we get about half the survival benefit as seen in humans who get surgery/XRT/TMZ, if we normalize for lifespan (using survival of the mice with U87 as a survival reference). This is promising, because we eventually expect our method to be used in combination with routine clinical GBM therapy approaches (*i.e.*, surgery, XRT, and TMZ), and our other survival studies show longer survival for U87 mice treated with both photothermal therapy and chemotherapy (Supplementary Fig. 41). We also observed much longer survival in immunocompetent mice (Supplementary Fig. 42).

Perspectives and potential clinical impacts

Recent studies have shown that photothermal treatment of brain cancers with gold nanostars can trigger immune responses [12] and this effect can be potentially used to enhance the treatment efficacy of our approach, due to improved recognition of the tumor by the immune system. Higher temperature elevations can be achieved by increasing the nanostar concentration in the tumor or irradiating them with higher optical powers, and necessary safety and tolerability studies would need to be performed in Phase 1 human trials. We also envision more advantages in real clinical therapeutic scenarios, which are often initiated by standard-of-care resection of the tumors. GBM resection not only helps to prolong the survival due to debulking, but also provides a window of opportunity for implantation of our devices in tumor cavities for effective photothermal treatment of any post-operative residual tumor or tumors recurring at shorter irradiation distances. This can be achieved mainly because of the high tissue penetration rate of the electromagnetic power that we use for wireless activation of our devices. Alternative strategies such as designing devices with series of light sources that emit higher optical powers with longer emission wavelengths (which have higher tissue penetration rates), as well as coupling our devices with guiding lenses (*e.g.*, GRIN lenses [13]) can also be used to deliver the light to deeper distances inside the brain. Also, light sources can be connected to the antenna which is implanted on the skull and then be guided to the tumors at different depths in the human brain [14,15]. Additionally, we envision that the next generation of wireless photothermal therapy devices would be equipped with LEDs emitting higher wavelengths (*i.e.*, more than 1000 nm) and higher optical powers, as well as higher electrical to optical power transformation efficiencies, which would permit the treatment of larger

and deeper tumors. Finally, the number of LEDs can be increased for more power transfer and increasing the irradiation volume in the human brain.

In a clinical setting, measuring the actual temperature of the tumor and optical output of the LEDs is crucial to determine the safest and most effective treatment plan and parameters. Multiple approaches can be used to achieve a closed-loop dosimetry system. For example, measurement of harmonic signals backscattered during the treatment can provide an estimate of the optical power being delivered. The nonlinearity of the LEDs results in a harmonically rich backscatter signal from the antenna which can be used as a reference to determine and tune required optical power levels [16]. Alternatively, when the wireless device is implemented on a silicon chip to achieve a smaller size and better operation flexibility, an optical sensor and a temperature sensor can be embedded on-chip, providing an accurate measurement of both the temperature and the optical power levels. The measurements can be transmitted back to a central hub which can adjust the output power levels of the transmitter. Other techniques such as combination of brain MRI with biophysical modeling can also be used for measuring the temperature in human brain [17].

Additionally, our wireless photothermal therapy method is not limited to the gold nanostars shown in this work, and different formulations of nanoparticles with various morphologies for enhanced photothermal response can be developed for more effective photothermal therapy efficacy at lower optical powers (*i.e.*, deeper tissues). Other types of nanoparticles with tuned morphologies, hydrodynamic sizes, surface chemistries, biocompatibility and specific tumor targeting capabilities can also be designed to improve therapeutic efficacy and long-term safety of this approach for applications in the brain or other organs. We used intratumoral administration in this study since the blood brain barrier (BBB) limits the amount of nanoparticles that accumulate in the brain tumors after their intravenous administration. Also, unlike conventional intravenous injection, intratumoral administration of such a low dosage of the nanoparticles eliminates side-effects on other organs such as liver and spleen and is made possible because surgical resection is standard of care in patients with glioblastoma. Methods such as using high intensity focused ultrasound can be used to open the BBB and possibly increase the amount of the nanoparticles extravasating into tumors for sufficient photothermal response. Also, biodegradable nanoparticles with prolonged blood circulation half-life and higher photothermal responses (*i.e.*, generating significantly higher photothermal heat at much lower concentrations in the tumors) can be

designed to enable our wireless therapy method followed by intravenous administration of the nanoparticles.

This versatile technique paves the way for development of a wide range of electro-optical therapeutic platforms to facilitate management of different tumors, including those which are impossible to resect, due to their risky anatomical location (*e.g.*, inoperable deep brain tumors). Our wireless platform can be feasibly programmed to initiate and terminate the photothermal therapeutic action with desired radiation intensities and wavelengths. Also, NIR radiation enables treatment of deeper tumors, due to their high rates of tissue penetration. Unlike conventional radiation and chemotherapy approaches, this new cancer therapy toolbox does not impose unavoidable side-effects on surrounding healthy tissues and other parts of the body. This method is not limited to nanoparticles for heat generation and can be tuned to enhance therapy through optical response of any other type of molecules such as NIR-responding photosensitizer molecules in photodynamic therapy.

References:

1 Chen, Y., Xu, C., Cheng, Y. & Cheng, Q. Photostability enhancement of silica-coated gold nanostars for photoacoustic imaging guided photothermal therapy. *Photoacoustics* **23**, 100284, doi:10.1016/j.pacs.2021.100284 (2021).

2 Furube, A. & Hashimoto, S. Insight into plasmonic hot-electron transfer and plasmon molecular drive: new dimensions in energy conversion and nanofabrication. *NPG Asia Materials* **9**, e454 (2017).

3 Wang, M., Kim, M., Xia, F. & Xu, C. Impact of the emission wavelengths on in vivo multiphoton imaging of mouse brains. *Biomed Opt Express* **10**, 1905-1918, doi:10.1364/BOE.10.001905 (2019).

4 Stujenske, J. M., Spellman, T. & Gordon, J. A. Modeling the Spatiotemporal Dynamics of Light and Heat Propagation for In Vivo Optogenetics. *Cell Rep* **12**, 525-534, doi:10.1016/j.celrep.2015.06.036 (2015).

5 Barnett, R. E., Liu, J. & Lazar, S. A RF to DC Voltage Conversion Model for Multi-Stage Rectifiers in UHF RFID Transponders. *IEEE Journal of Solid-State Circuits* **44**, 354-370 (2009).

6 U.S. FCC, 47 CFR 1.1310, Radiofrequency radiation exposure limits. Federal Communications Commission, Washington, DC.

7 Wei, Q. *et al.* Intraoperative Assessment and Photothermal Ablation of the Tumor Margins Using Gold Nanoparticles. *Advanced Science* **8**, 2002788 (2021).

8 Bastiancich, C., Da Silva, A. & Esteve, M. A. Photothermal Therapy for the Treatment of Glioblastoma: Potential and Preclinical Challenges. *Front Oncol* **10**, 610356, doi:10.3389/fonc.2020.610356 (2020).

9 Stupp, R. *et al.* Effect of Tumor-Treating Fields Plus Maintenance Temozolomide vs Maintenance Temozolomide Alone on Survival in Patients With Glioblastoma: A Randomized Clinical Trial. *JAMA* **318**, 2306-2316, doi:10.1001/jama.2017.18718 (2017).

10 Simpson, J. R. *et al.* Influence of location and extent of surgical resection on survival of patients with glioblastoma multiforme: results of three consecutive Radiation Therapy Oncology Group (RTOG) clinical trials. *Int J Radiat Oncol Biol Phys* **26**, 239-244, doi:10.1016/0360-3016(93)90203-8 (1993).

11 Holland, J. M., Mitchell, T. J., Gipson, L. C. & Whitaker, M. S. Survival and cause of death in aging germfree athymic nude and normal inbred C3Hf/He mice. *J Natl Cancer Inst* **61**, 1357-1361, doi:10.1093/jnci/61.5.1357 (1978).

12 Liu, Y. *et al.* Plasmonic gold nanostar-mediated photothermal immunotherapy for brain tumor ablation and immunologic memory. *Immunotherapy* **11**, 1293-1302, doi:10.2217/imt-2019-0023 (2019).

13 Barbera, G., Liang, B., Zhang, L., Li, Y. & Lin, D. T. A wireless miniScope for deep brain imaging in freely moving mice. *J Neurosci Methods* **323**, 56-60, doi:10.1016/j.jneumeth.2019.05.008 (2019).

14 Montgomery, K. L. *et al.* Wirelessly powered, fully internal optogenetics for brain, spinal and peripheral circuits in mice. *Nat Methods* **12**, 969-974, doi:10.1038/nmeth.3536 (2015).

15 Ausra, J. *et al.* Wireless, battery-free, subdermally implantable platforms for transcranial and long-range optogenetics in freely moving animals. *Proc Natl Acad Sci U S A* **118**, doi:10.1073/pnas.2025775118 (2021).

16 Bansal, A., Yang, F., Xi, T., Zhang, Y. & Ho, J. S. In vivo wireless photonic photodynamic therapy. *Proc Natl Acad Sci U S A* **115**, 1469-1474, doi:10.1073/pnas.1717552115 (2018).

17 Sung, D. *et al.* Personalized predictions and non-invasive imaging of human brain temperature. *Communications Physics* **4**, 1-10 (2021).

Supplementary Figures:

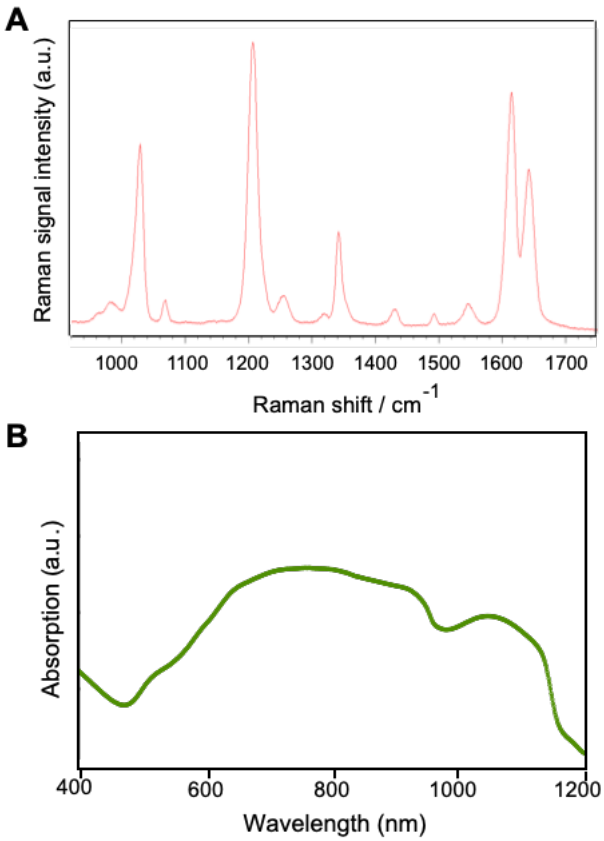

Fig. S1. Optical characterization of the gold nanoparticles used for photothermal heating of the brain tumors. (**A**) Raman spectrum and (**B**) UV-vis absorption spectrum of the nanoparticles. Raman spectrum was used to generate the Raman images shown in Supplementary Figs. 3-4.

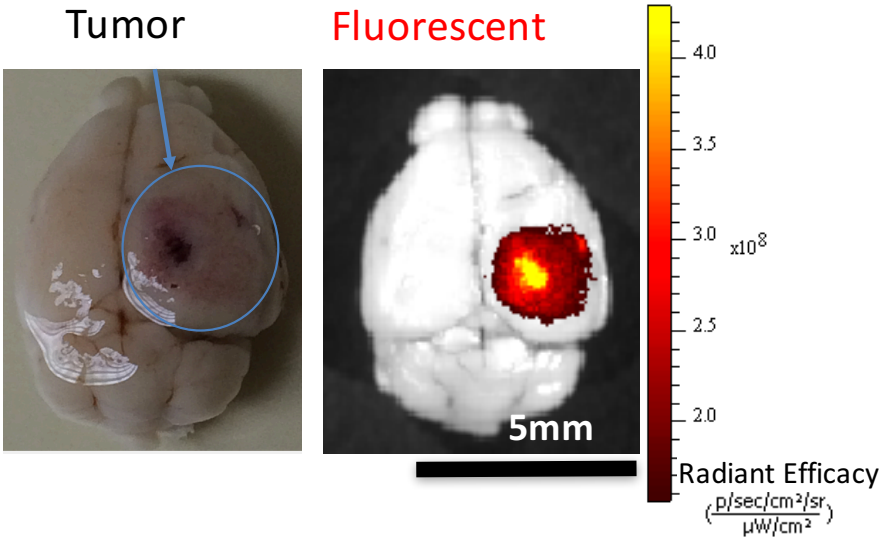

Fig. S2. Intratumoral diffusion of administered nanoparticles. *Ex vivo* near infra-red fluorescence (NIRF) image of a representative mouse brain after intratumoral injection of the nanoparticles. Photograph of the brain is shown on the left for comparison. Histology and NIRF images of the brain slices are shown in Fig. 1I-J.

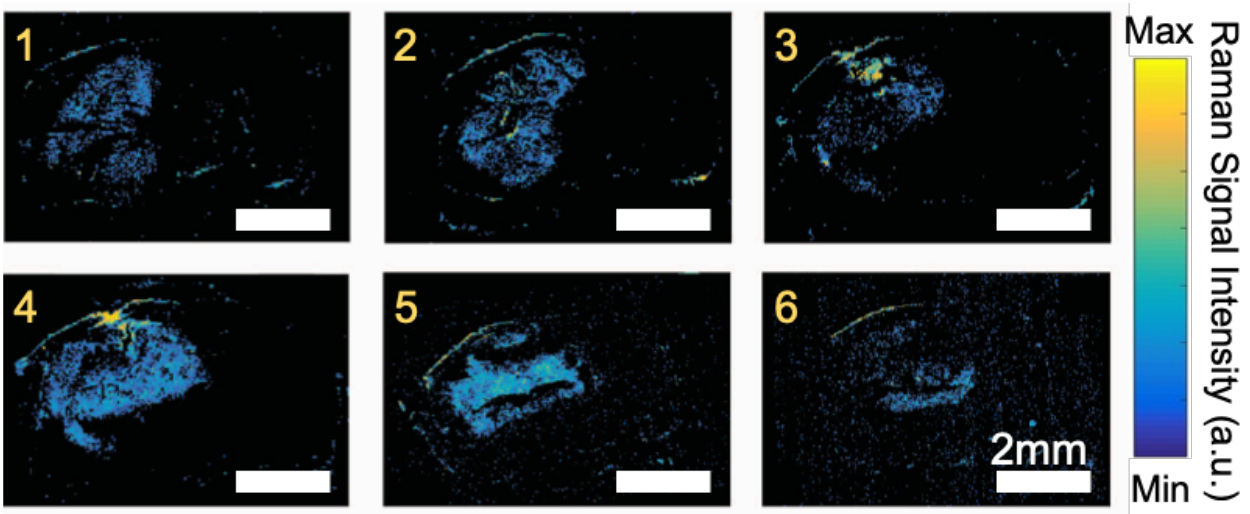

Fig. S3. Raman image of the brain slices. Counterpart surface enhanced raman (SERS) images of the slices shown in Fig. 1J, further confirming selective diffusion of the nanoparticles in tumors. Raman signals are specifically related to SERS effect of the nanoparticles and images were generated using the Raman spectrum of the nanoparticles shown in Supplementary Fig. 1A.

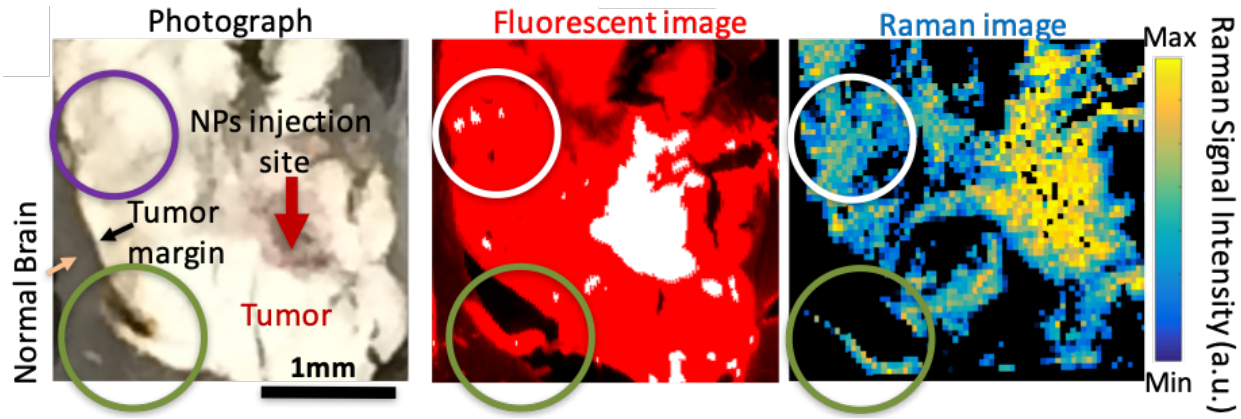

Fig. S4. Fluorescent and Raman images of a brain section. High magnification photograph (left), near infra-red fluorescence (NIRF, middle), and surface enhanced Raman (SERS, right) images of a brain section, used to verify co-localization of the fluorescent and SERS signals of the nanoparticles in tumor. Images confirm the nanoparticles specific diffusion exclusively within the tumor. Two selected regions at the interface between the tumor and normal brain (white and green circles) show matching of the nanoparticles signals in fluorescent and Raman images. Note that injection site contains a higher concentration of the nanoparticles, resulting in higher NIRF and Raman signal intensities.

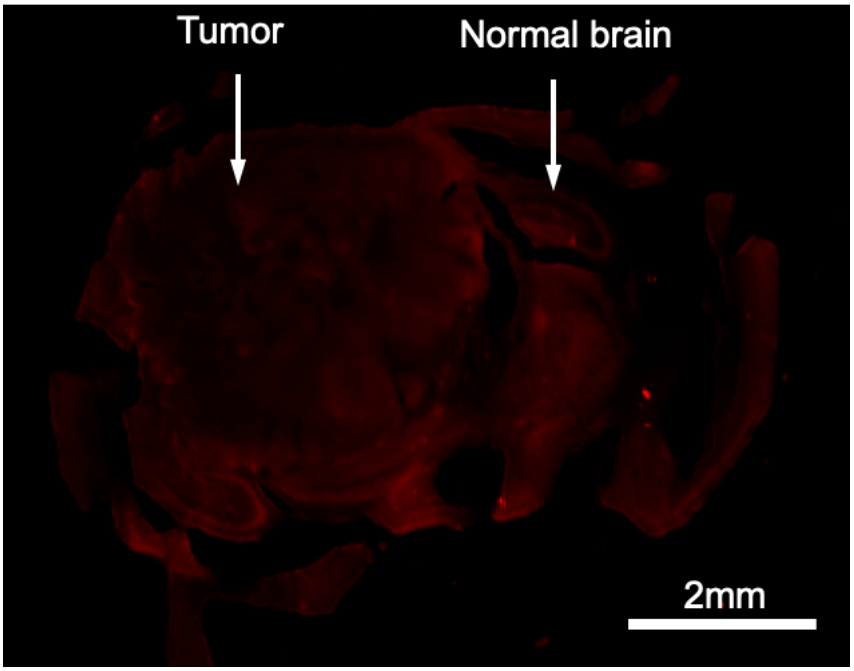

Fig. S5. Fluorescent image of control brains without any nanoparticles injection. Near infrared fluorescence (NIRF) image of a brain slice obtained from a control mouse after injection of PBS (1×). Tumor tissue does not generate noticeable autofluorescent signal compared with the adjacent normal brain tissue, confirming that the fluorescent signal in Fig. 1J was solely generated from the intratumorally injected nanoparticles.

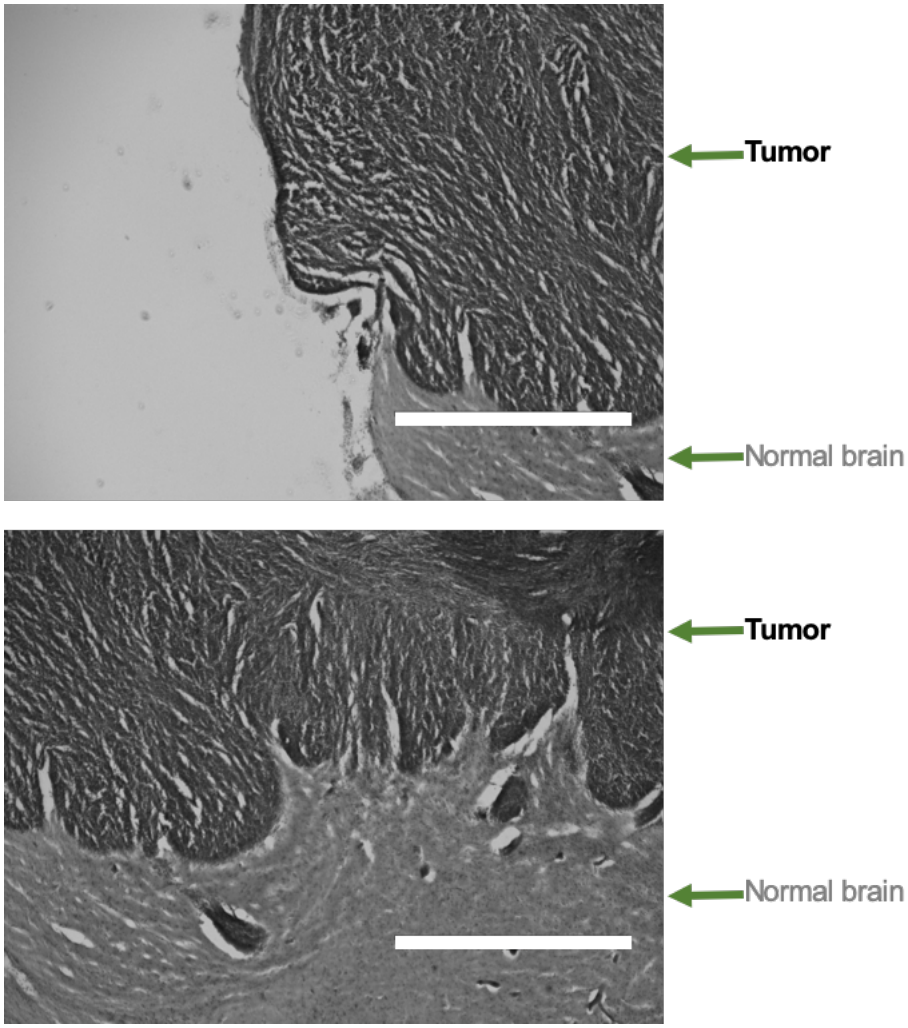

Fig. S6. Light microscopy of the brain slices. Two representative images from H&E stained brain tissue sections showing the interconnected microporous structure of the tumor compared with adjacent normal brain tissue. This distinct microstructure facilitated selective diffusion of the nanoparticles in tumor (see Fig. 1J and Supplementary Figs. 2-5). All scale bars represent 1 mm.

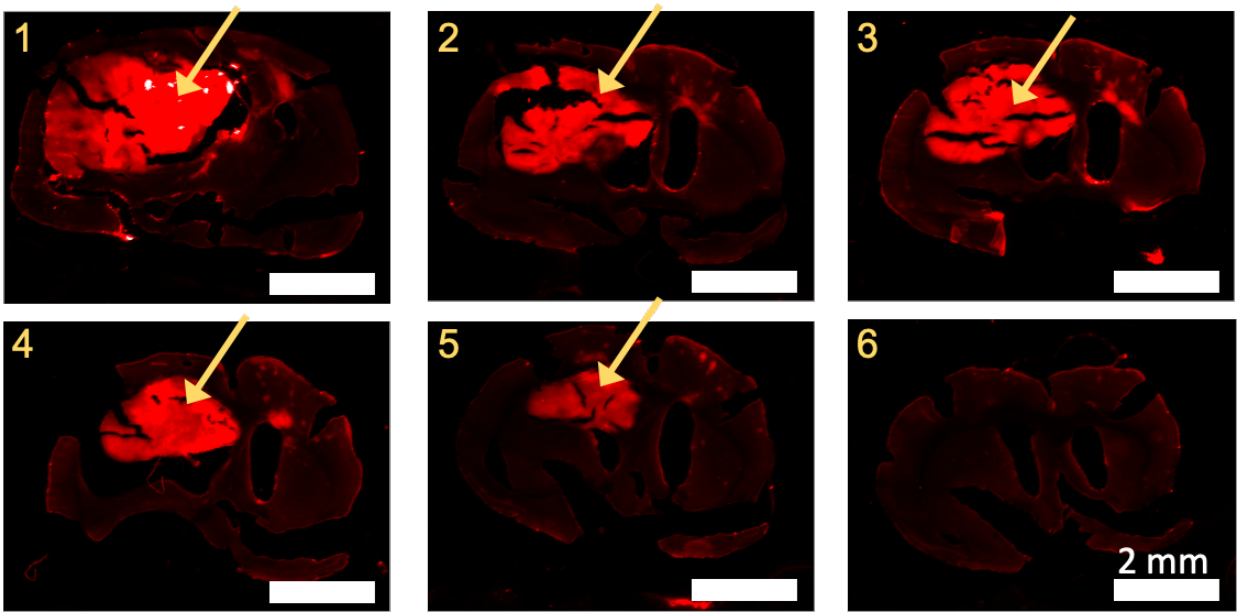

Fig. S7. Nanostars retention in tumor tissues. Fluorescent images of the consecutive brain slices at 300 µm distances from each other, obtained from a mouse with U87 tumor at the end of the wireless photothermal treatment. The major part of the nanostars (red) were retained in tumor tissues (shown with arrows) during the whole treatment period due to their enhanced permeation and retention (EPR) effect.

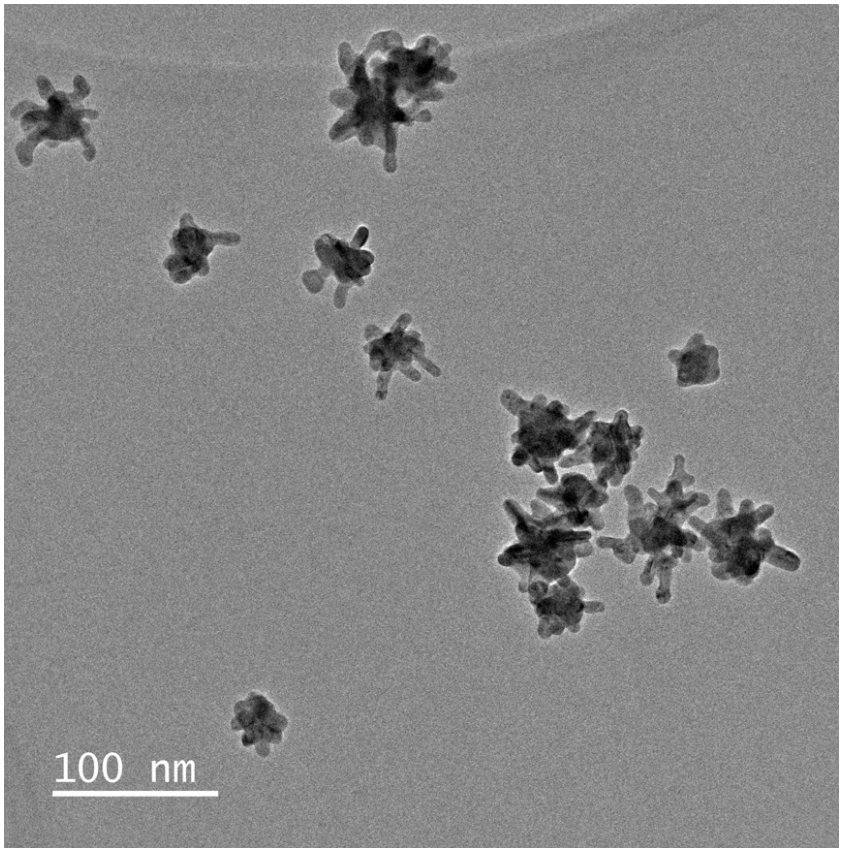

Fig. S8. Nanostars stability after long-term irradiation. TEM image of the nanostars after irradiation with a 940-nm LED at high power level (-4 dBm) for 15 min/day over a period of 15 days. Nanostars also retained their photothermal efficacy during this period, as verified by thermal imaging of the nanoparticles under long-term pulsed irradiation.

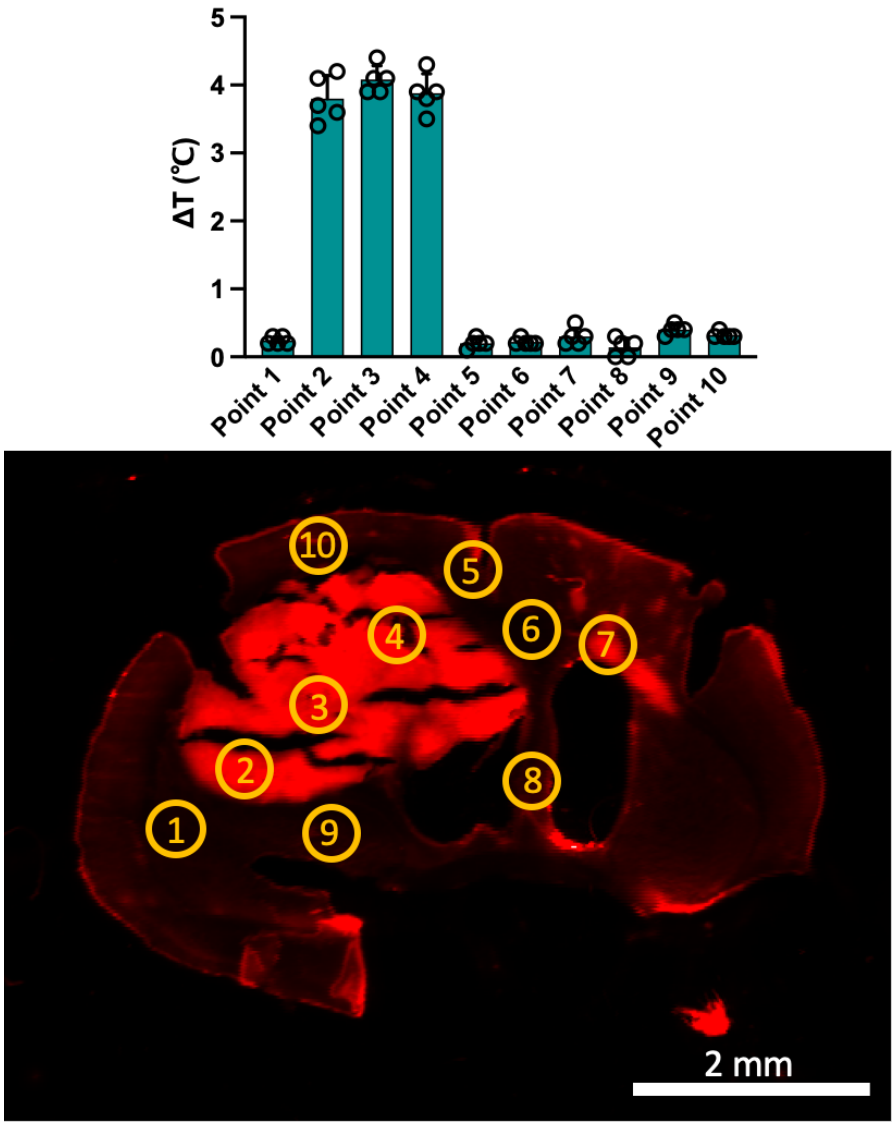

Fig. S9. Temperature variations in a brain slice under irradiation. 810-nm device was fixed (~45° angle and ~3.5 mm distance) above the brain slice (placed horizontally at h = 3 cm above the center of the TX coil) and the tumor area was irradiated using the high power levels described in Supplementary Fig. 30. Temperatures at different locations of the brain slice were recorded and compared in the graph bar. Fluorescent image shows distribution of the nanostars in the tumor (see Supplementary Fig. 7 for details). Temperature elevation was significantly higher inside the tumor zone (points 2, 3, and 4), when compared with adjacent normal brain tissues (points 1, 5, 6, 7, 8, 9, and 10). h = 3 cm was used to resemble distance of the implanted devices from the TX coil in *in vivo* studies.

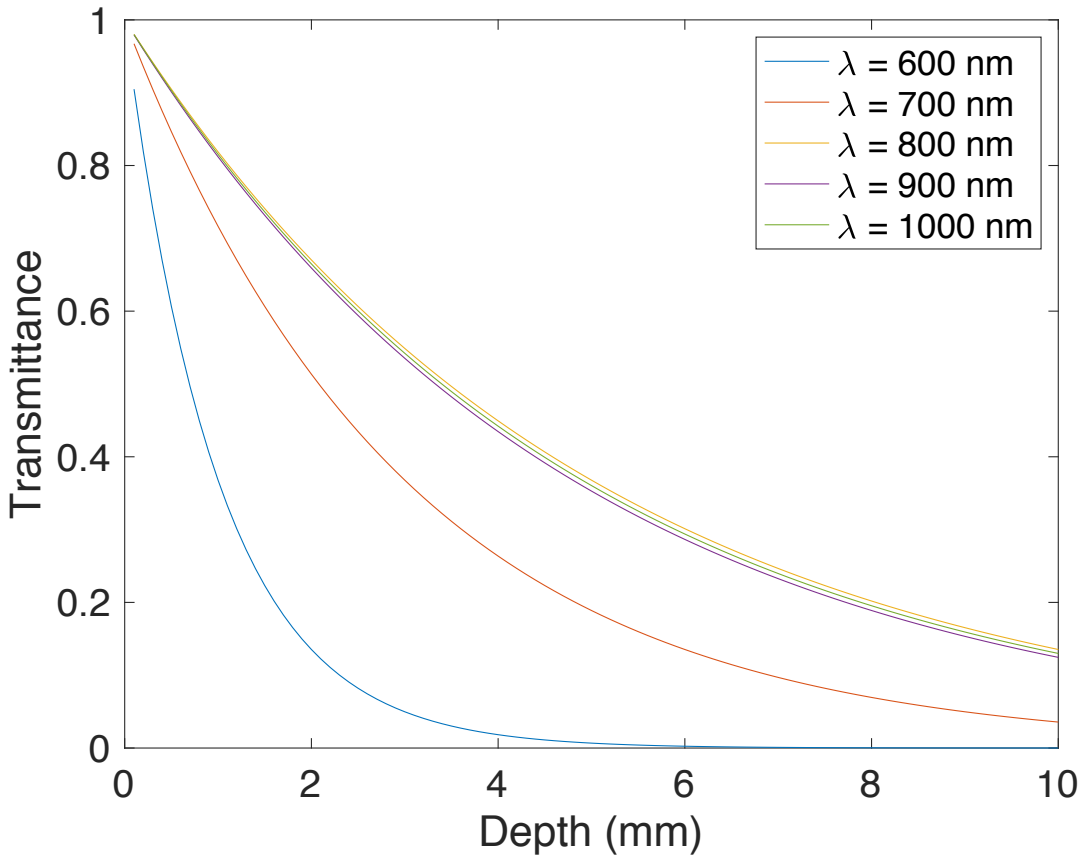

Fig. S10. Attenuation pattern of the light in mouse brain. We used light diffusion theory and Beer-Lambert exponential decay model to estimate light transport in the brain at different wavelengths. See Supplementary Text for details.

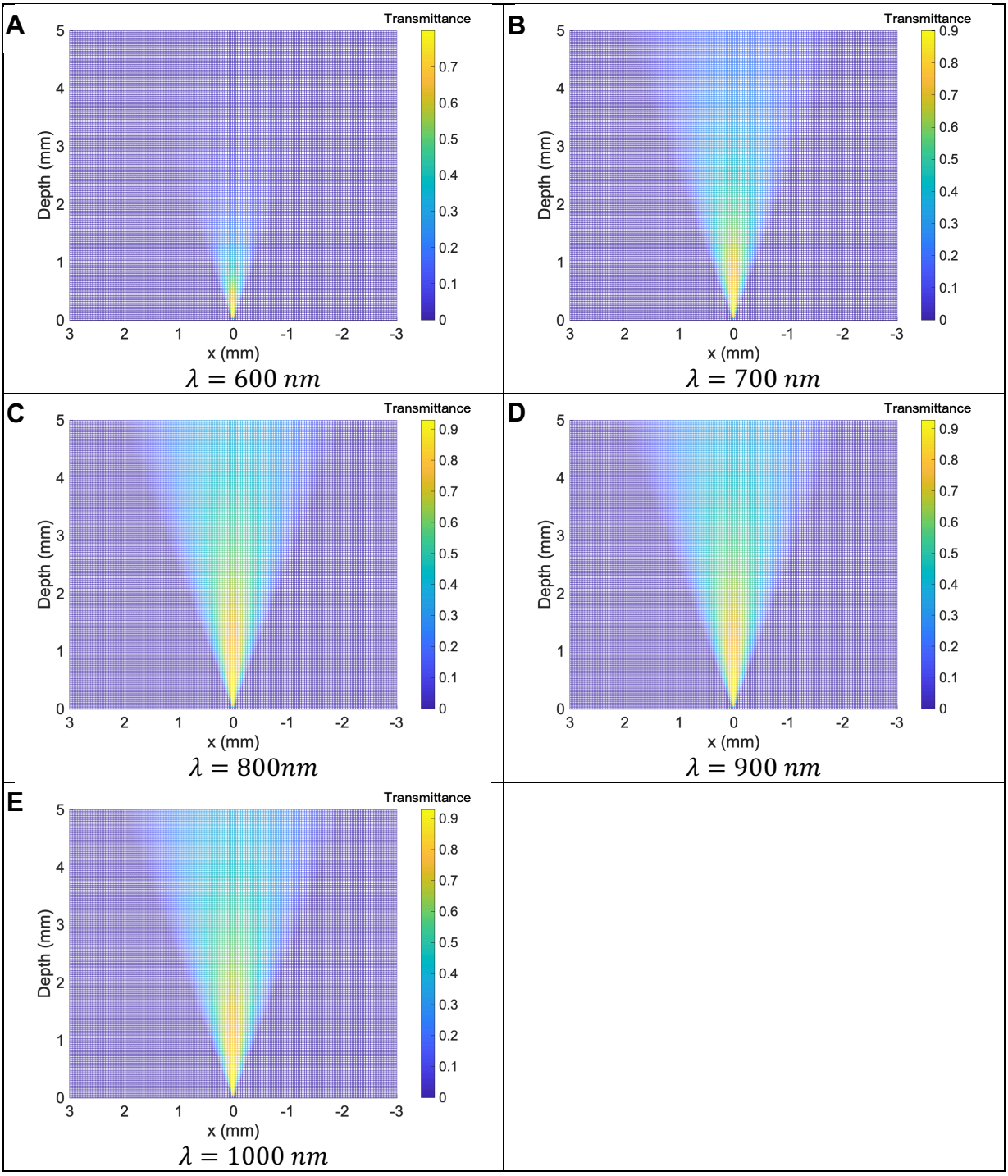
A
Transmittance
Depth (mm)
x (mm)
$\lambda = 600\ nm$
B
Transmittance
Depth (mm)
x (mm)
$\lambda = 700\ nm$
C
Transmittance
Depth (mm)
x (mm)
$\lambda = 800nm$
D
Transmittance
Depth (mm)
x (mm)
$\lambda = 900\ nm$
E
Transmittance
Depth (mm)
x (mm)
$\lambda = 1000\ nm$

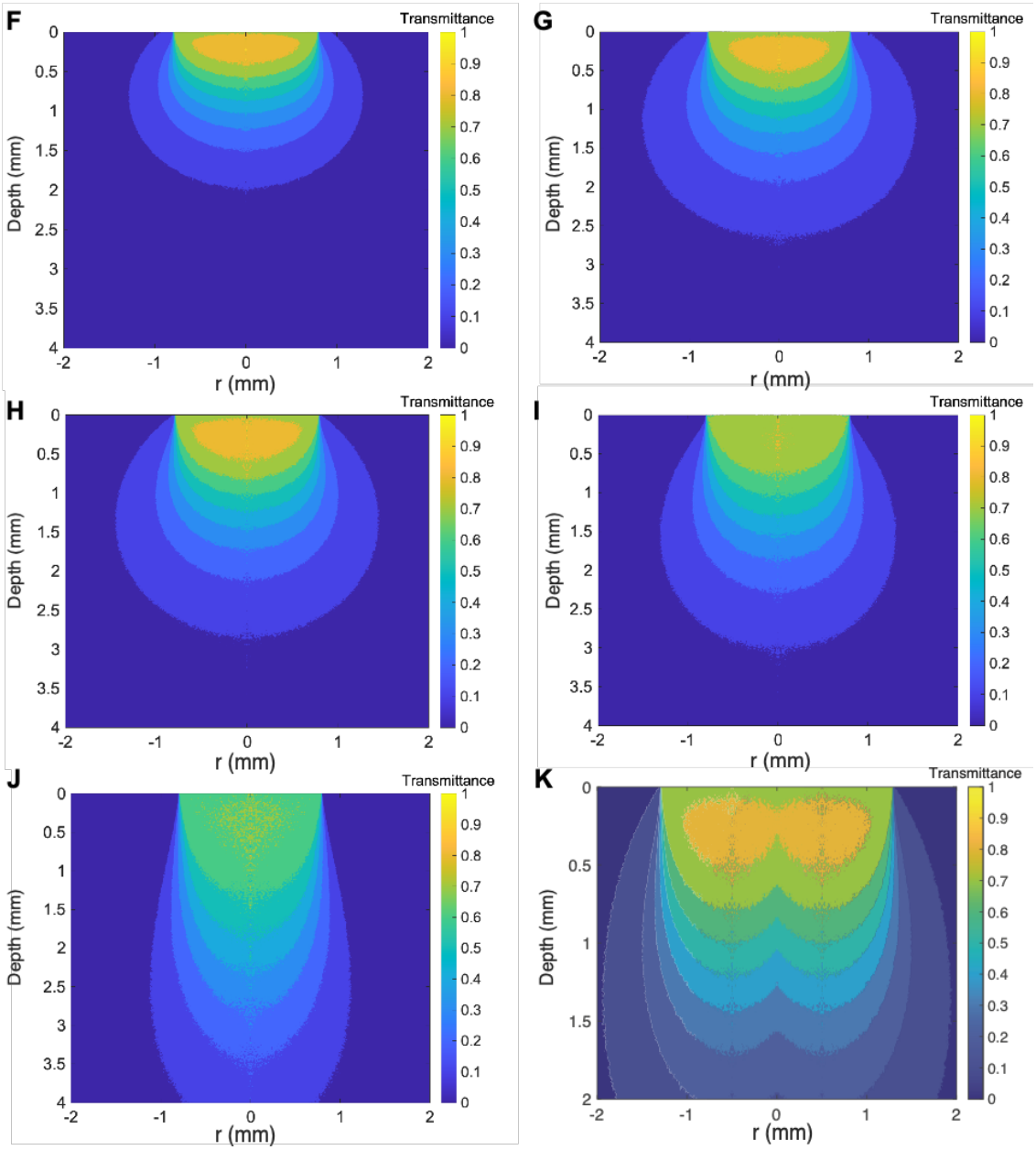

Fig. S11. Two dimensional light transmittance as a function of wavelength. (A-E) Transmittance ($I(z)/I_0$, where I_0 is the light intensity at the LED surface) in the mouse brain, when one LED is on, determined using Beer-Lambert light diffusion model. Here, we assumed each LED as a planar light source placed on top of the tissue at x = 0 and z = 0, radiating downward toward the brain tumors. (F-J) Iso-contour areas representing transmittance in the mouse brain, as a function of distance from the LEDs, estimated by Monte Carlo simulation for comparison. LEDs are considered as point light sources in this model and ellipsoid-shape graphs in (F) to (J) represent light intensity variations for 600, 800, 950, 1100, and 1400 nm wavelengths. Note that our devices had two LEDs at a distance of ~ 1 mm from each other which doubled the irradiated zone in the brain. Irradiation zone when two 950 nm LEDs are on simultaneously are shown in (K) for comparison. See Supplementary Text for modeling details.

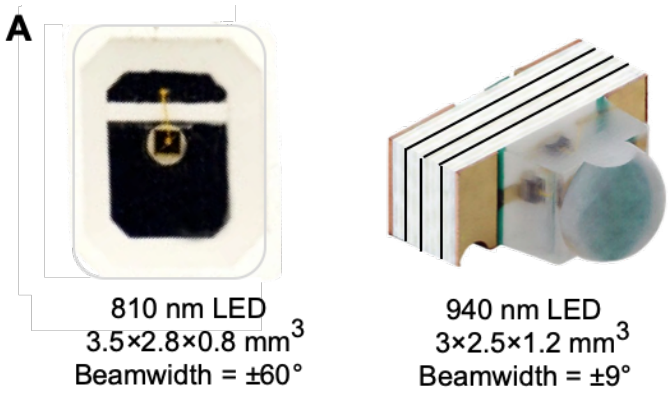

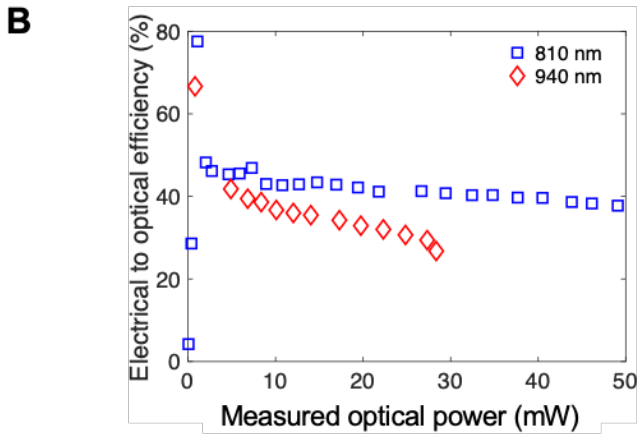

C

	Maximum forward current (I_{MAX})	Radiated power	Forward voltage	Reverse voltage	Calculated efficiency	Measured efficiency
LED / Units	**mA**	**mW @ I_{MAX}**	**V**	**V**	**%**	**%**
810 nm	100	55*	1.4	5	40	40
940 nm	70	40	1.5	5	38	38

Fig. S12. Characterization of the LEDs used for wireless photothermal therapy. (**A**) Photographs showing the 810-nm and 940-nm LEDs used in this study, along with their dimensions (L×W×H) and half beam width. (**B**) Measured efficiency of the 810- and 940-nm LEDs for generating NIR beams with different optical powers. (**C**) Electrical parameters of the LEDs from the datasheet. The ideal efficiency of each LED was calculated using the data provided by the manufacturers, by assuming a linear scaling of optical power with forward current. The calculated results were in agreement with the measured data. 810-nm and 940-nm LEDs had different I_{max} rating, which limited their maximum allowable electrical power and therefore, their maximum optical power. * Estimated based on similar LEDs from the vendors and our measurements.

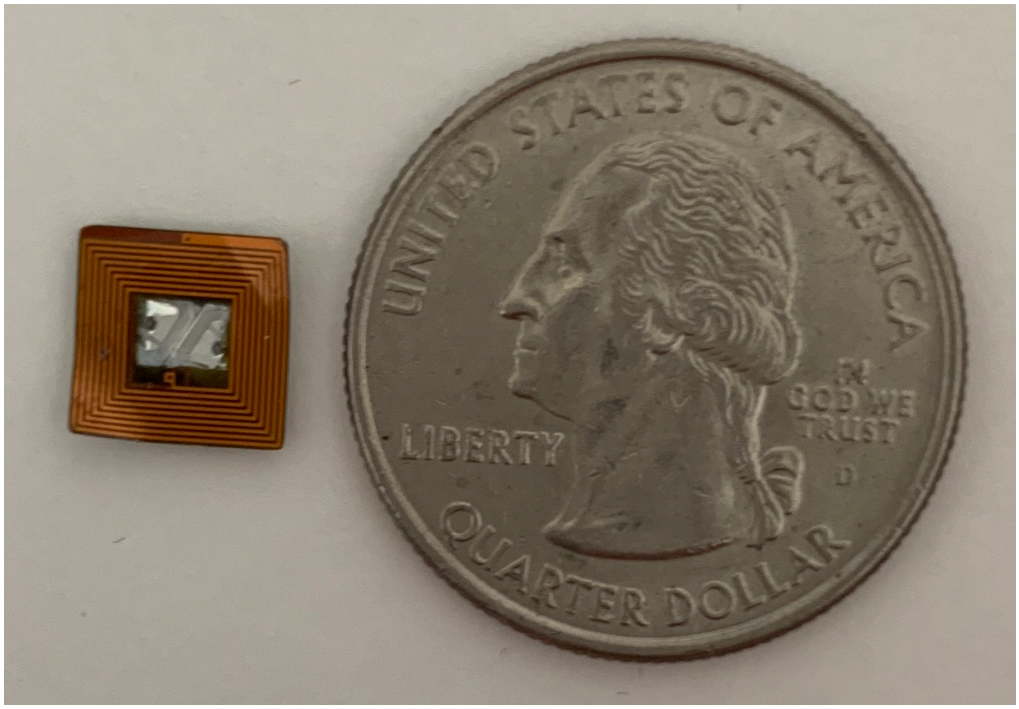

Fig. S13. Evaluation of the device size. Photograph to compare the size of our devices with a quarter dollar coin.

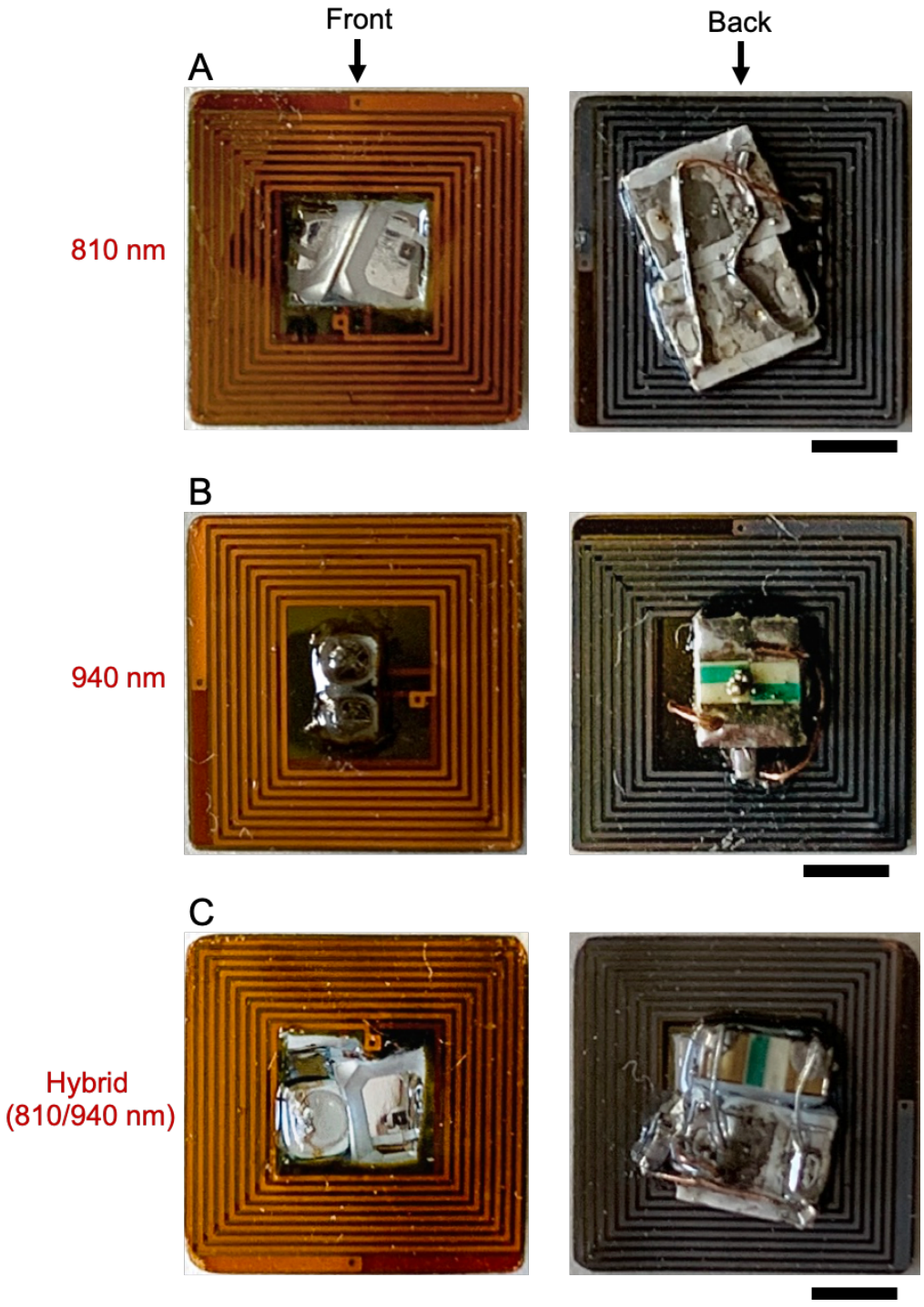

Fig. S14. Photographs showing frontside and backside of different designs of the NIR-emitting devices. (**A** and **B**) Devices with two 810-nm or 940-nm back-to-back connected LEDs. (**C**) A hybrid device with both 810- and 940-nm LEDs showing versatility of our design to illuminate tissues with different wavelengths. Matching components (*i.e.*, capacitors) and LEDs were soldered on the back of the flexible antenna board. Thickness of the central parts of the devices were ~1 and 1.5 mm in in (A), and (B-C), respectively. Scale bars represent 2 mm.

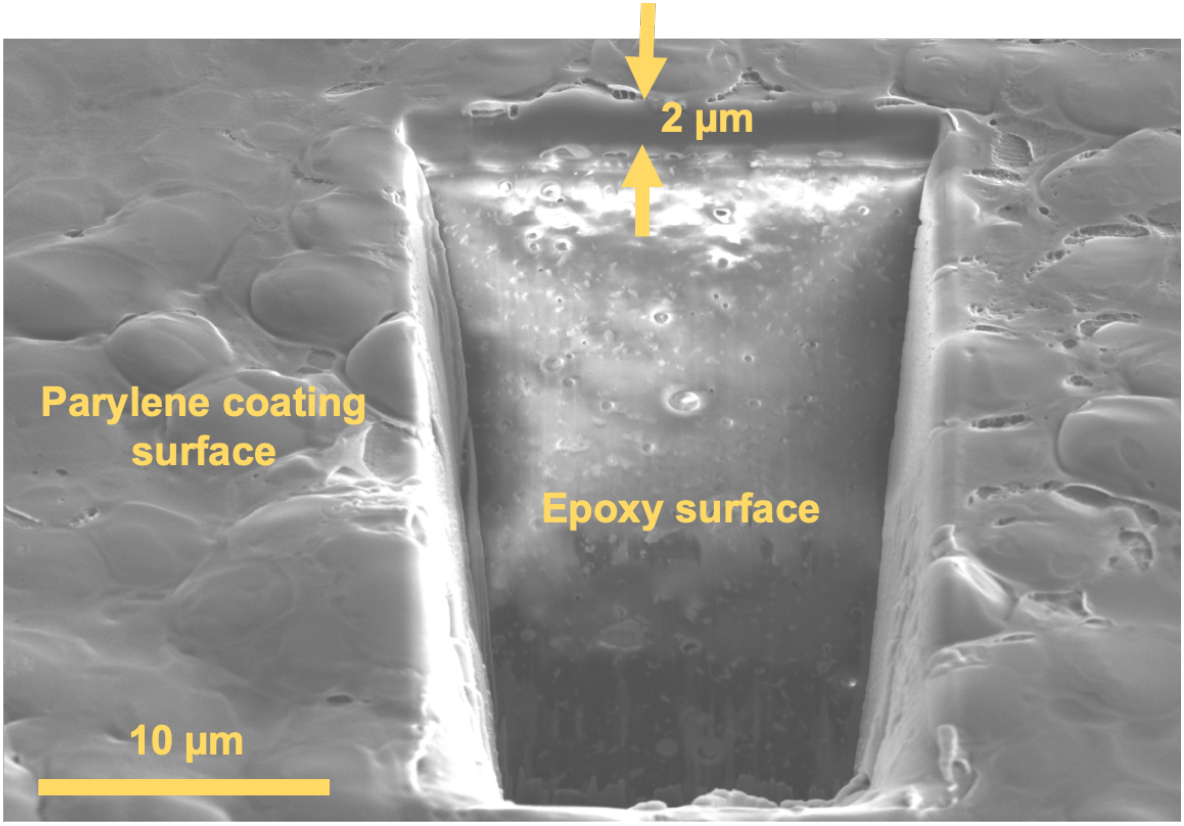

Fig. S15. Analysis of the surface coating of the devices. Higher magnification scanning electron microscopy (SEM) image from the surface of a device before implantation (also see Fig. 2C), confirming deposition of a 2-µm thick parylene layer on the device to prolong it's *in vivo* life-time. A wedge-like area was removed from the surface of the device using focused ion beam (FIB) to reveal the thickness of the parylene coating.

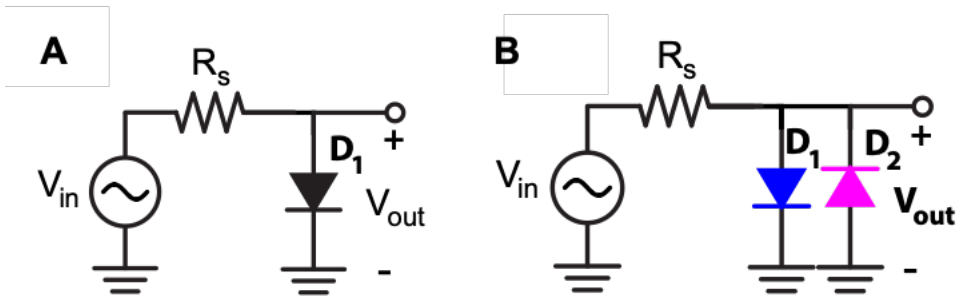

Fig. S16. Two possible device designs which use the rectifying capability of the LED as a diode. (**A**) Single and (**B**) back-to-back LED topologies.

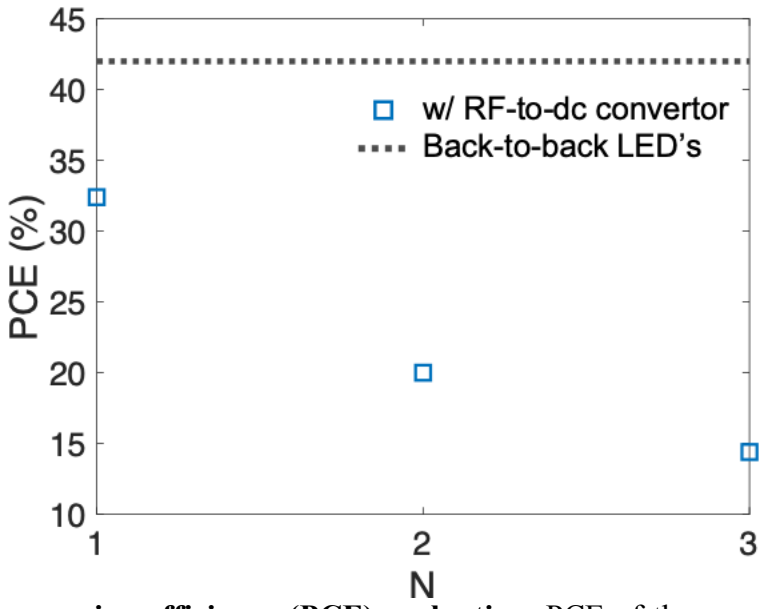

Fig. S17. Power conversion efficiency (PCE) evaluation. PCE of the conventional RF-to-DC converter approach with 1 to 3 stages compared to the back-to-back LED topology, suggesting the latter achieves a better PCE.

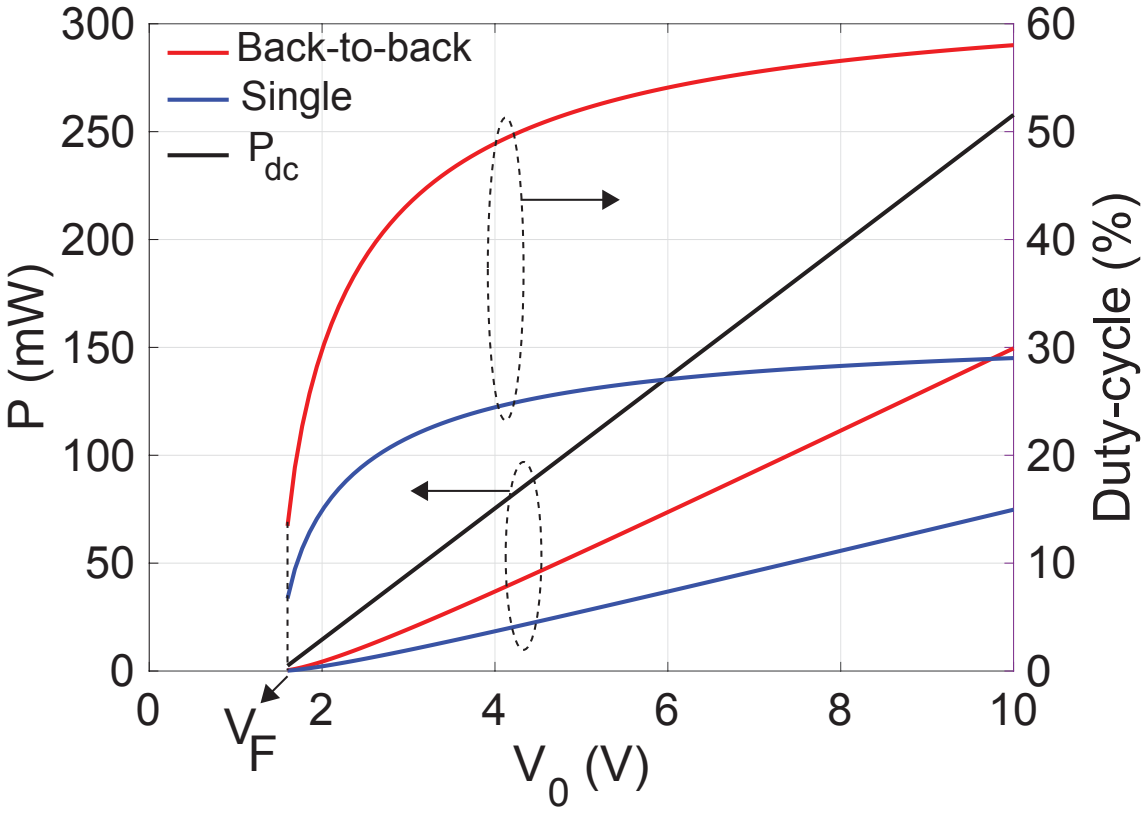

Fig. S18. Evaluating duty-cycled NIR-emitting devices. The average power delivered to the LEDs in single LED and back-to-back LED designs, as well as the equivalent DC power (P_{dc}). These results further verified that choosing a V0 larger than 4 V could not help to increase the duty-cycle considerably, and therefore was not necessary to achieve higher photothermal effects in the brain.

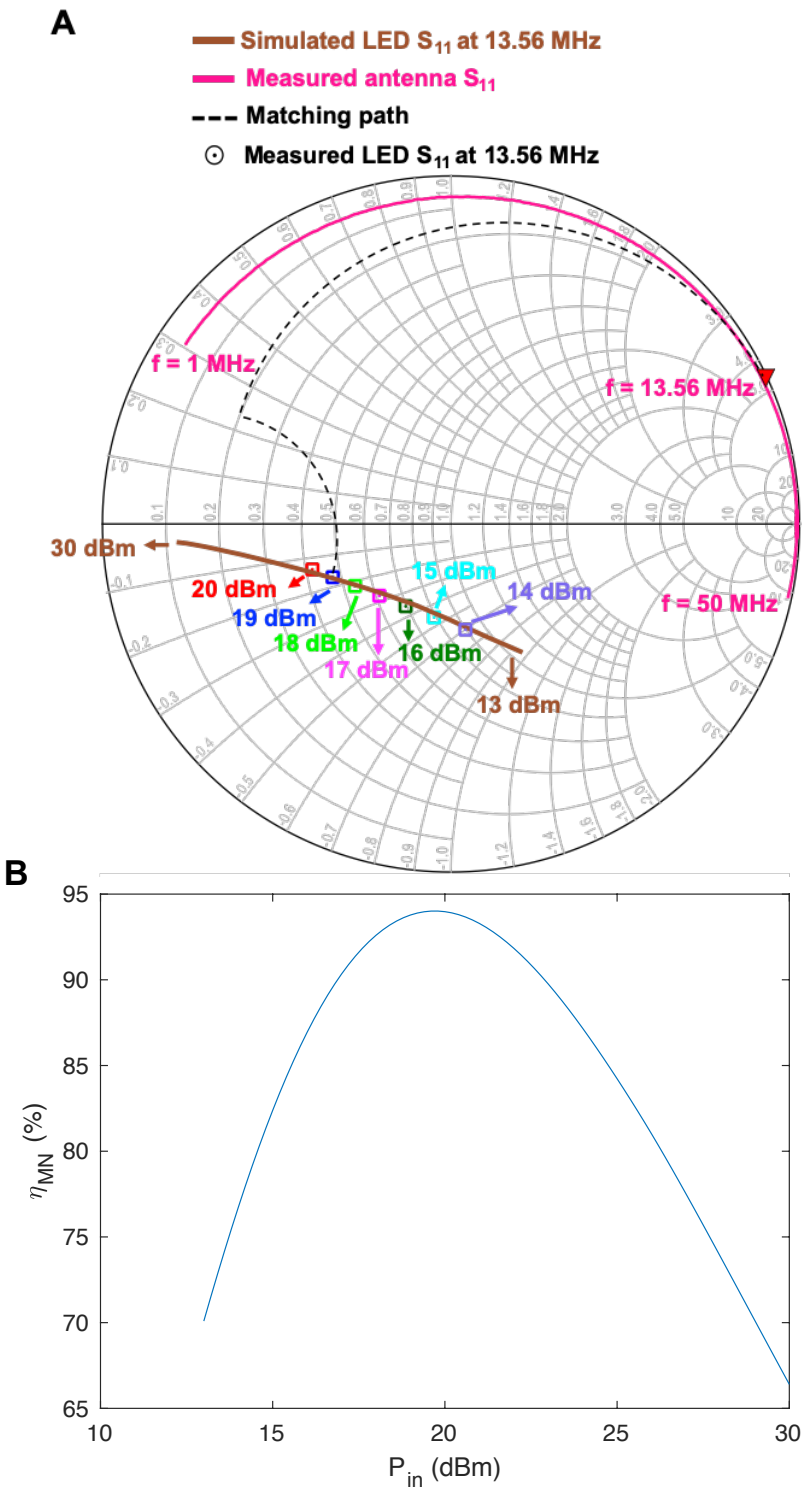

Fig. S19. RF characterization of the back-to-back 940 nm LEDs. (**A**) The measured (square data points) and simulated (solid brown line) impedance profile of the back-to-back 940-nm LEDs at different power levels (13-30 dBm), along with the antenna S_{11}. The dashed line shows the matching path at 13.56 MHz. Matching was done with high-Q capacitors. (**B**) Variation of η_{MN} with input power.

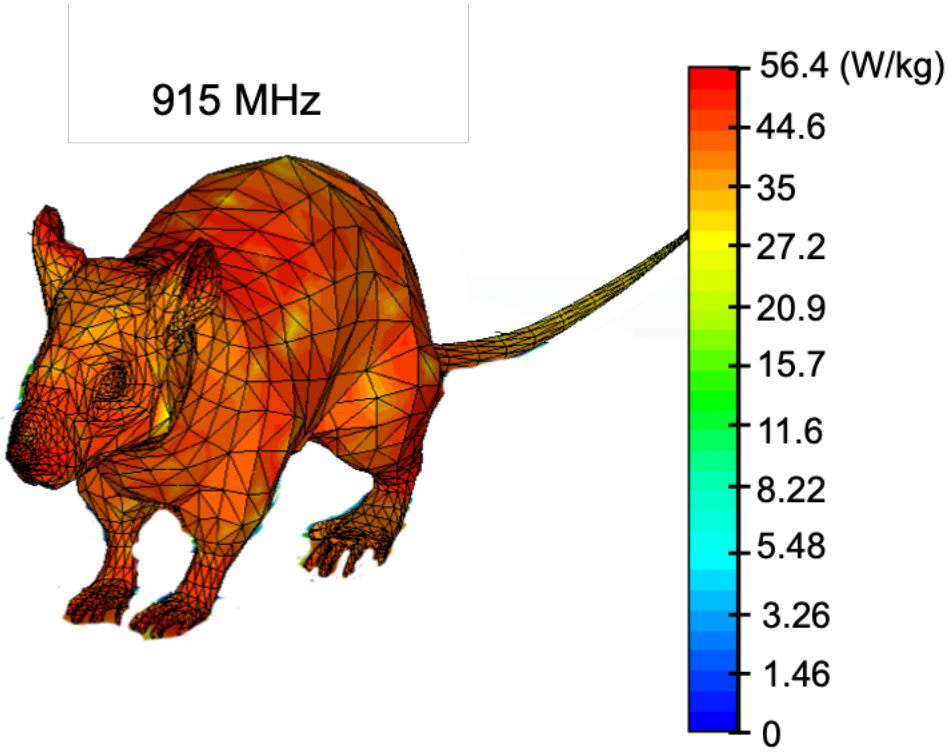

Fig. S20. SAR simulation at 915 MHz (FF range). The 1-g SAR value at this frequency was 56.4 W/kg, when the highest power level (38 dBm) was used. This is significantly higher than the 1-g SAR value calculated for 13.56 MHz (See Fig. 3D), indicating that using 915 MHz for wireless power transfer was not safe per FCC regulations. The scale bar is logarithmic.

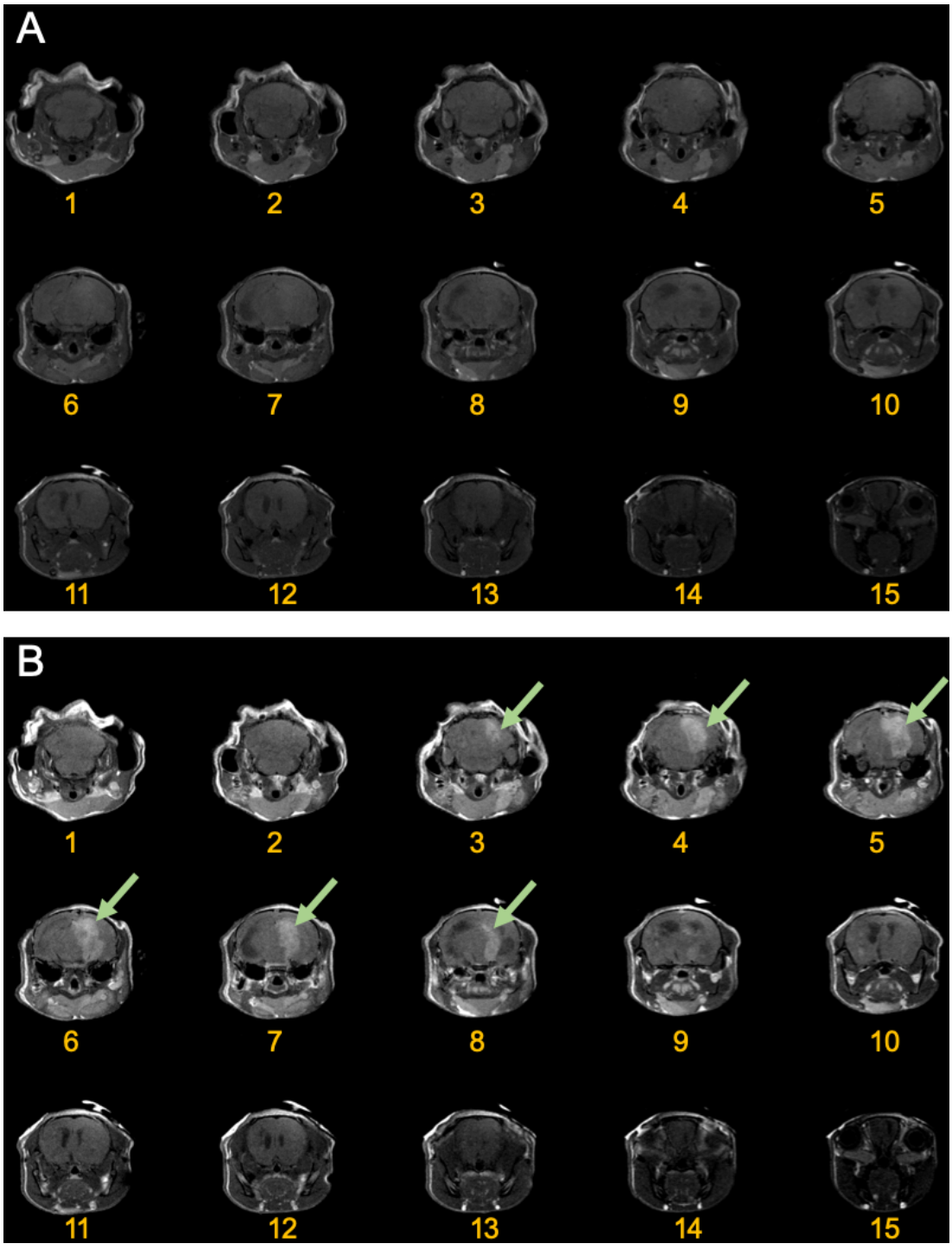

Fig. S21. Monitoring tumor size and anatomical location. (**A** and **B**) T1-weighted MRI of a mouse brain before and after injection of Gd-contrast. 15 consecutive brain slices (1 mm thick) are shown in each panel. Orthotopic brain tumors are shown with arrows in (B). Images of consecutive slices were used to calculate the approximate tumor volume, as a criteria for injecting the nanoparticles. MRI was performed ~2-3 weeks after intracranial implantation of the human U87-eGFP-fLuc glioblastoma cells. Images are shown from caudal (slice 1) to rostral (slice 15).

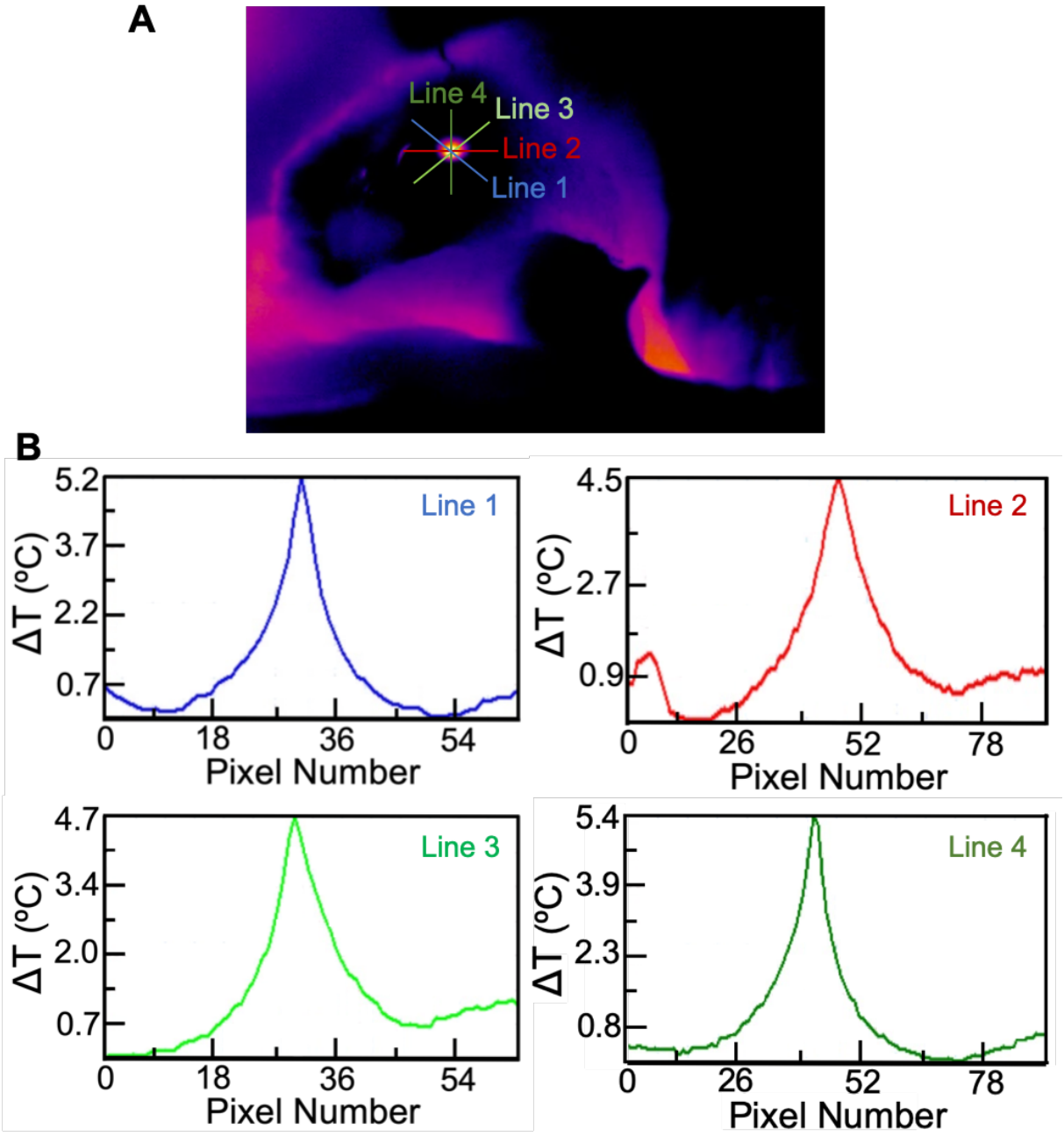

Fig. S22. Thermal analysis of the photothermal effects in tumor. (**A**) Thermal image showing photothermal heating effect of the nanoparticles (yellow bright spot) within the brain tumor in an anesthetized mouse. (**B**) Graphs showing temperature variation along Lines 1-4 shown in (A). Maximum temperature variations (ΔT ~ 4.5-5.4 ºC) were seen at the area directly irradiated with a focused NIR beam (bright spot in (A)). Also see Figs. 3F-G and Supplementary Fig. 23.

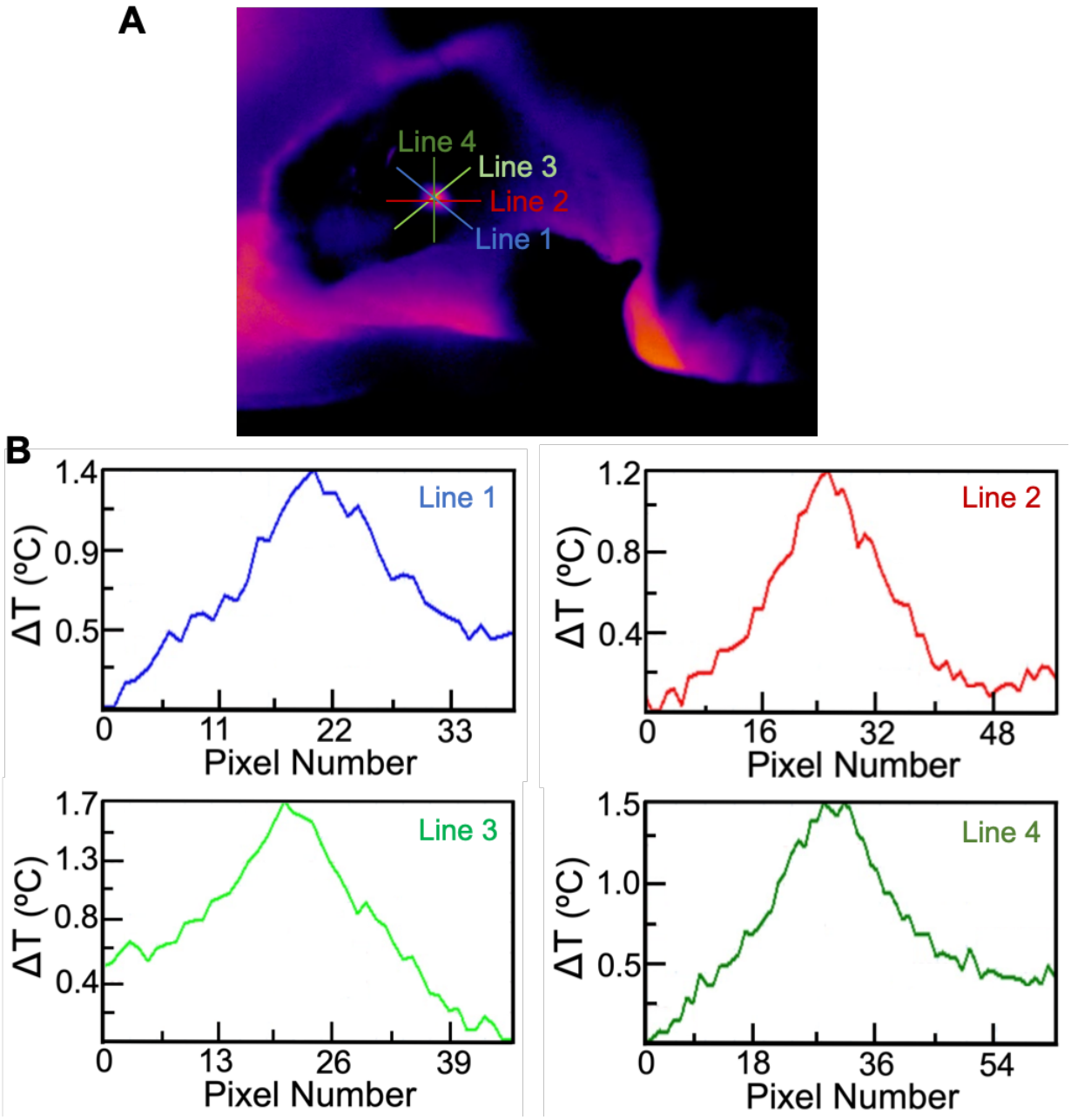

Fig. S23. Thermal effects at the marginal tumors adjacent to normal brain tissue. (**A**) *In vivo* thermal imaging shows heating profile at marginal areas of the tumor, where less nanoparticles were present. Note that highest concentration of nanoparticles were observed at the central part of the tumor (nanoparticles injection site). (**B**) Temperature variations along Lines 1-4 (ΔT ~ 1.2-1.5 ºC). Also see Supplementary Fig. 22.

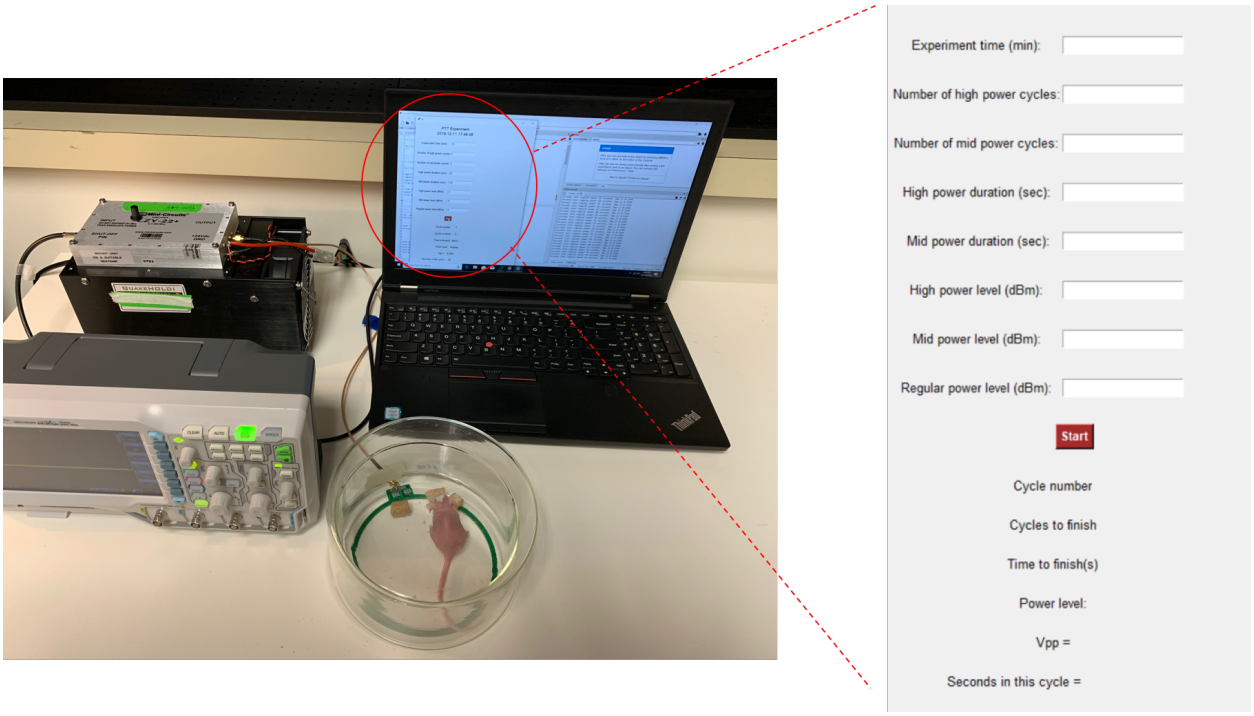

Fig. S24. Computer-controlled wireless powering graphical user interface (GUI). Snapshot of the GUI developed to input wireless photothermal therapy parameters (*i.e.*, number and duration of medium- and high-power cycles and the power levels) on a computer connected to our wirelessly-powered photothermal therapy setup.

Fig. S25. Treatment on freely-behaving animals. Representative photograph of a mouse doing normal activities (*e.g.*, eating) during the treatment in therapeutic chamber, indicating that our wireless photothermal treatment approach was not disturbing (also see Supplementary Video 1).

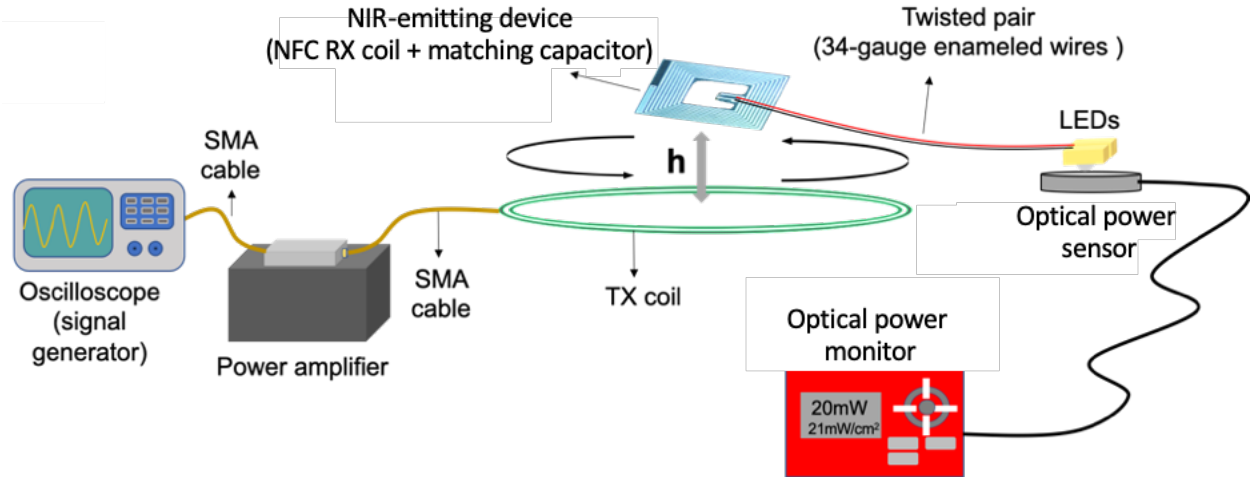

Fig. S26. Measuring optical emission powers at different distances between the TX coil and NIR device. Wireless powering and measurement setup used for determining optical power transformation efficiency of the devices at different vertical distances of 1, 2, 3, and 5 cm from the center of TX coil. The implanted devices were estimated to be within this distance range when freely-behaving mice were under wireless treatment in therapeutic chamber. Measured optical power values for different devices are shown in Fig. 4E and Supplementary Figs. 27 and 28. These measurements were done at the nominal RF power levels for each LED.

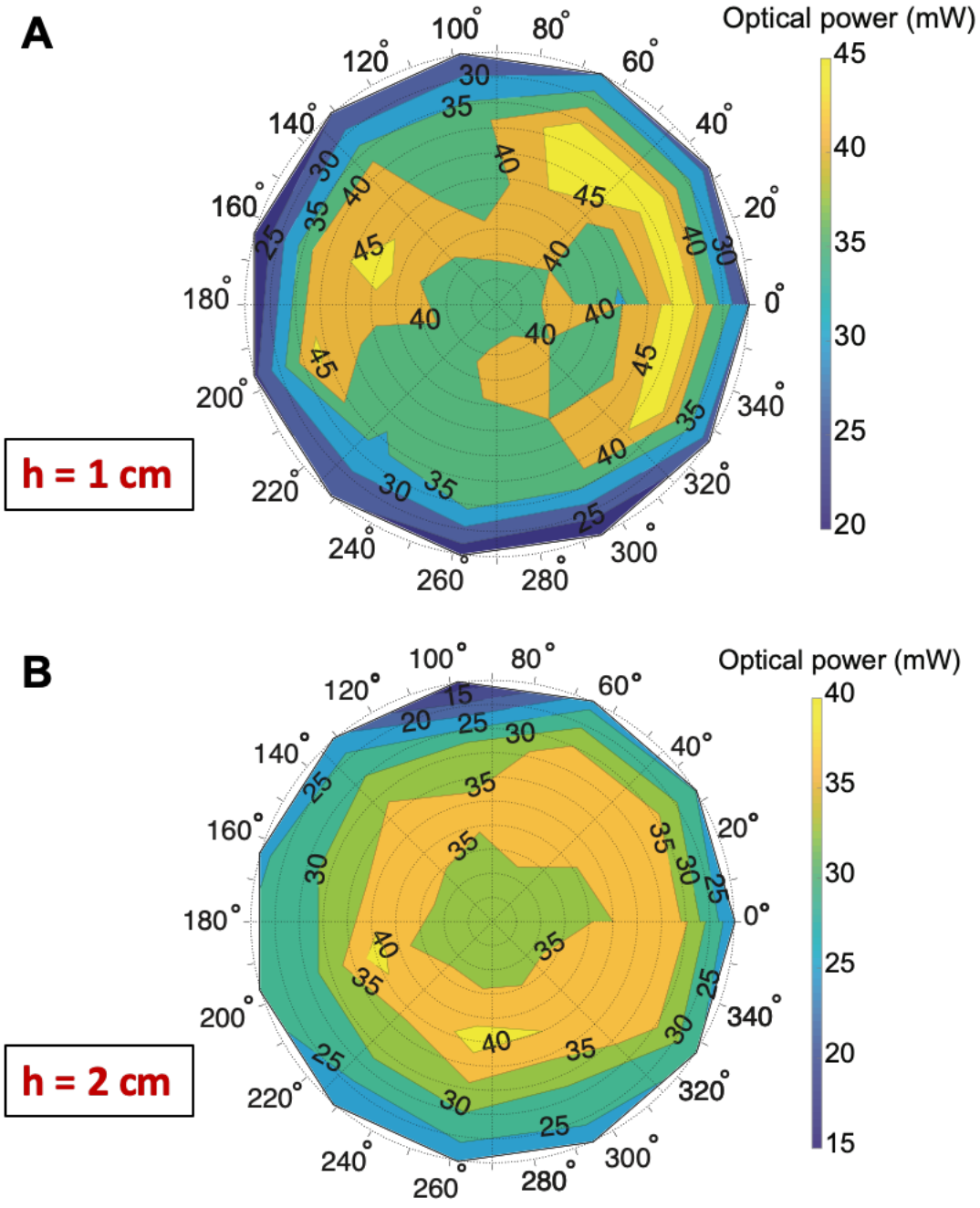
A
Optical power (mW)
45
40
35
30
25
20
h = 1 cm
B
Optical power (mW)
40
35
30
25
20
15
h = 2 cm

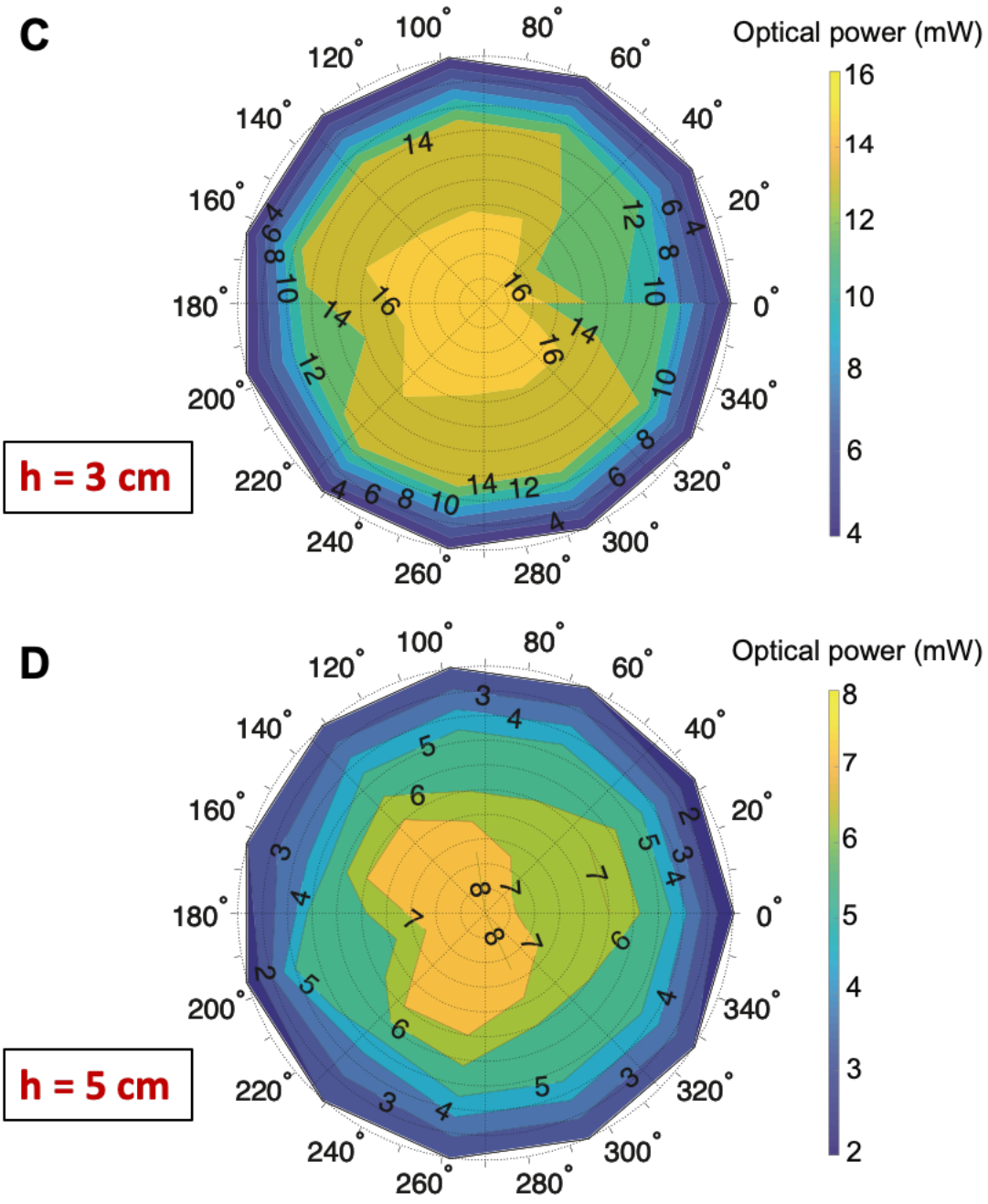

Fig. S27. Variations of optical powers obtained from wirelessly-powered 810-nm devices at different locations and heights in therapeutic chamber. Plots showing variations of optical power with distance from the center of the coil at different heights of (**A**) 1 cm, (**B**) 2 cm, (**C**) 3 cm, and (**D**) 5 cm. The radius of the transmitter coil was 6.15 cm. The wireless power transfer efficiency values are shown in Supplementary Fig. 29.

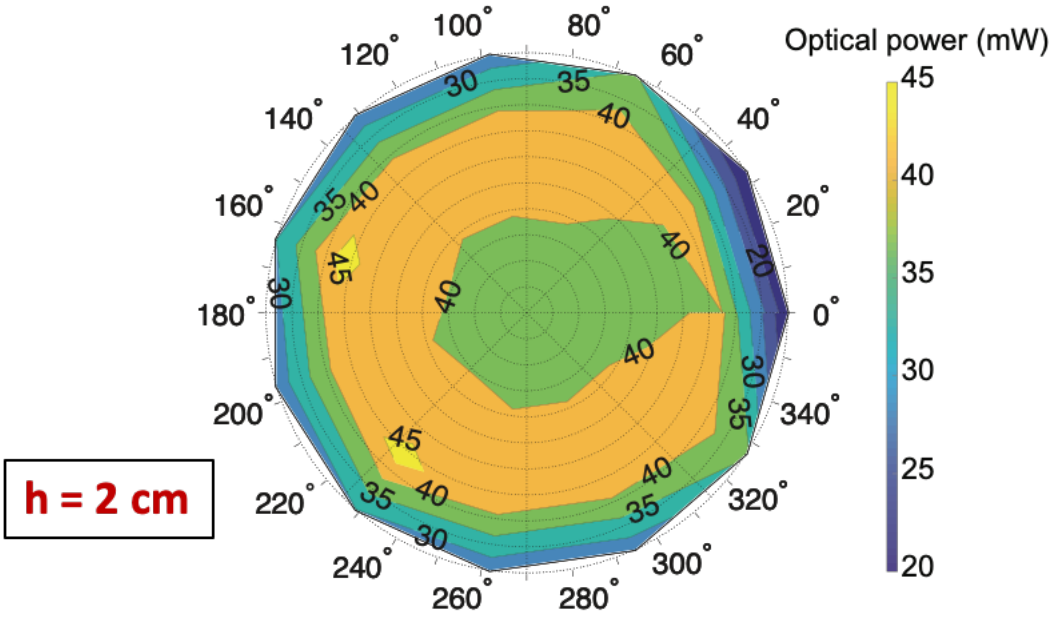

Fig. S28. Variations of optical powers obtained from wirelessly-powered 940-nm devices. Measurements were performed at 2 cm height relative to the transmitter (TX) coil. Measurements at 1, 3, and 5 cm heights are shown in Fig. 4E.

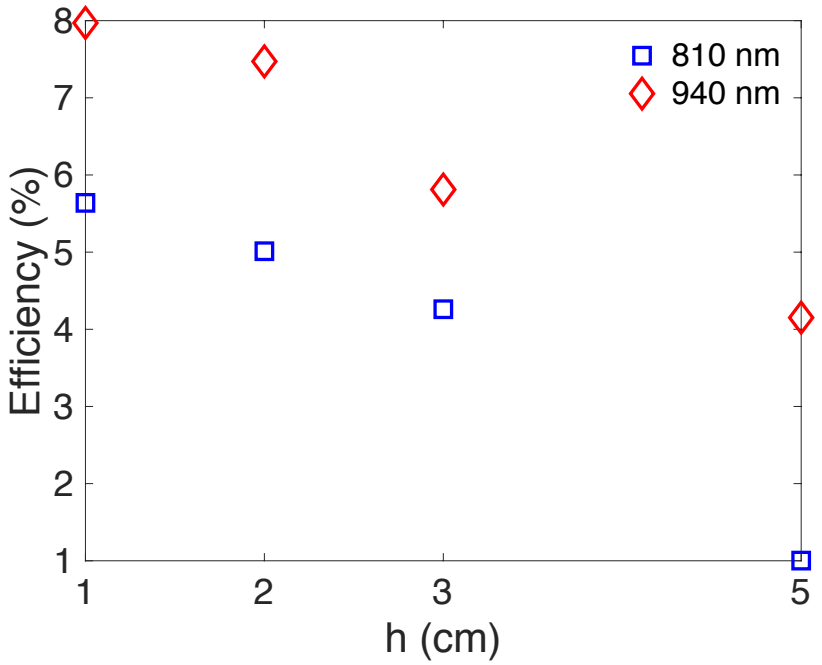

Fig. S29. Wireless power transfer efficiency. Overall wireless power transfer efficiency (from the output of the TX coil to the electrical power delivered to the LEDs) of the 810- and 940-nm devices at different heights, calculated from the optical power measurements in Fig. 4E, and Supplementary Figs. 27 and 28 (optical power maps) and using LEDs electrical-to-optical efficiency numbers shown in Supplementary Fig. 12. Generally, mice with large brain tumors are less active compared with healthy mice and our statistical behavioral analysis showed that the distance between an implanted device and the center of the TX coil was ~3 ± 0.5 cm more than 87% of time during the treatments. We considered this as the nominal height to obtain sufficient optical power for consistent and effective photothermal response of the nanoparticles (*i.e.*, ΔT ~ 3-5 ºC) in tumors during each treatment cycle.

A

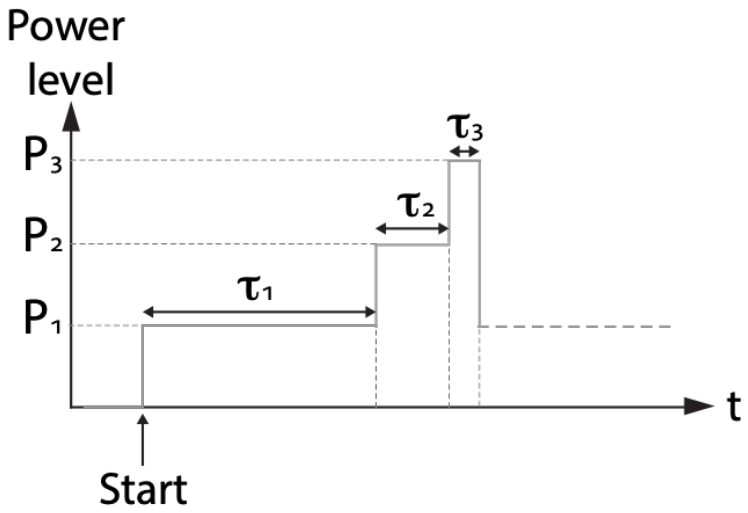

B

810 nm		940 nm	
Power Level	Duration	Power Level	Duration
$P_1 = -9\ dBm$	$\tau_1 = 7\ mins$	$P_1 = -10\ dBm$	$\tau_1 = 13\ mins$
$P_2 = -6dBm$	$\tau_2 = 5\ mins$	$P_2 = -7\ dBm$	$\tau_2 = 1\ mins$
$P_3 = -3\ dBm$	$\tau_3 = 3\ mins$	$P_3 = -4\ dBm$	$\tau_3 = 1\ mins$

Fig. S30. Multi-level wireless powering scheme for tumor treatments. (**A**) Diagram showing the therapy parameters (*i.e.*, wireless power levels and duration of each cycle) used for *in vivo* studies. During each time interval, a sinusoidal waveform at 13.56 MHz was used. (**B**) Power levels and pulse durations used for 810- and 940-nm devices. The output power of the transmitter P_1= 33 dBm, P_2= 36 dBm, and P_3= 39 dBm for 810-nm devices and P_1= 32 dBm, P_2= 35 dBm, and P_3= 38 dBm for 940-nm devices.

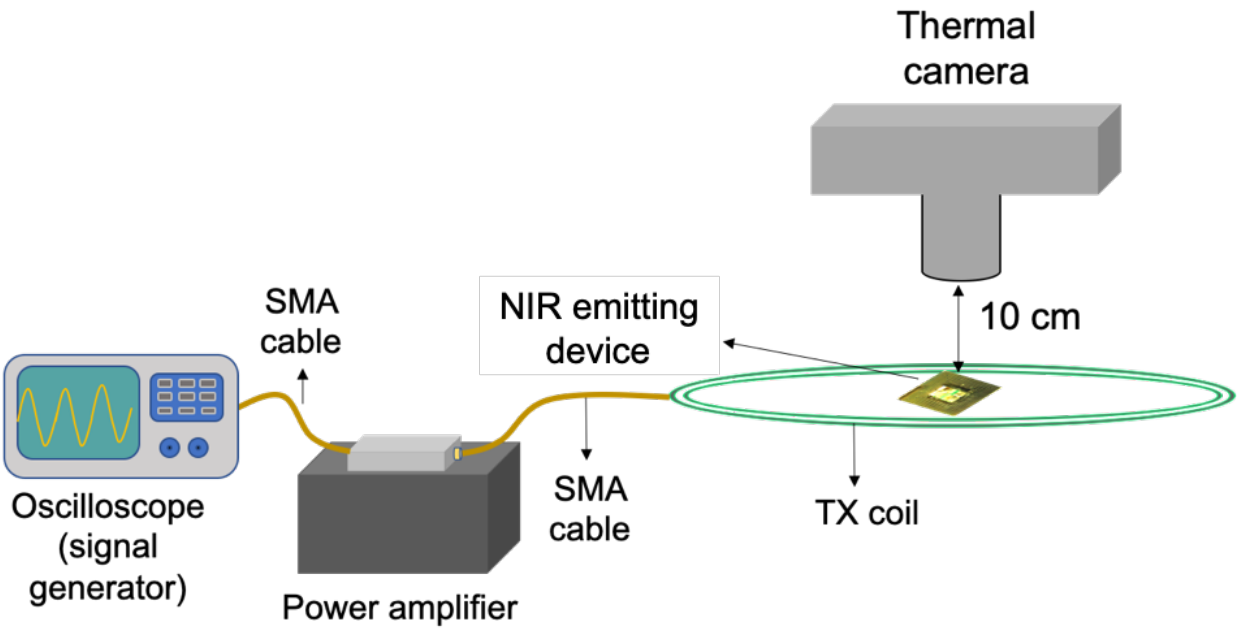

Fig. S31. Thermal imaging of the devices. Setup used for quantitative imaging of temperature variations on the wirelessly-powered NIR-emitting devices before their implantation. Results are shown in Fig. 1D and Supplementary Fig. 32.

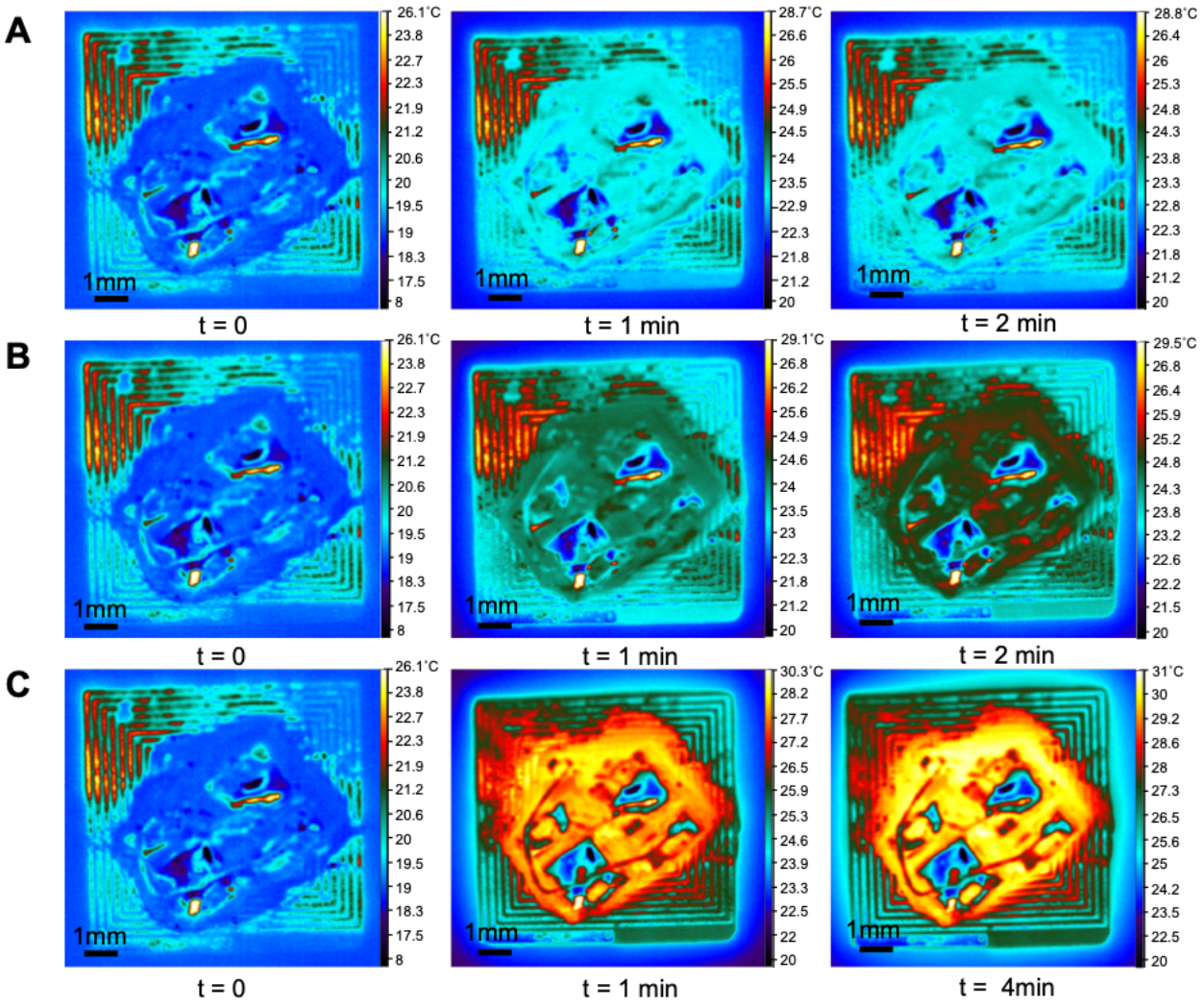
A
26.1°C
23.8
22.7
22.3
21.9
21.2
20.6
20
19.5
19
18.3
17.5
8
1mm
t = 0
28.7°C
26.6
26
25.5
24.9
24.5
24
23.5
22.9
22.3
21.8
21.2
20
1mm
t = 1 min
28.8°C
26.4
26
25.3
24.8
24.3
23.8
23.3
22.8
22.3
21.8
21.2
20
1mm
t = 2 min
B
26.1°C
23.8
22.7
22.3
21.9
21.2
20.6
20
19.5
19
18.3
17.5
8
1mm
t = 0
29.1°C
26.8
26.2
25.6
24.9
24.6
24
23.5
23
22.3
21.8
21.2
20
1mm
t = 1 min
29.5°C
26.8
26.4
25.9
25.2
24.8
24.3
23.8
23.2
22.6
22.2
21.5
20
1mm
t = 2 min
C
26.1°C
23.8
22.7
22.3
21.9
21.2
20.6
20
19.5
19
18.3
17.5
8
1mm
t = 0
30.3°C
28.2
27.7
27.2
26.5
25.9
25.3
24.6
23.9
23.3
22.5
22
20
1mm
t = 1 min
31°C
30
29.2
28.6
28
27.3
26.5
25.6
25
24.2
23.5
22.5
20
1mm
t = 4min

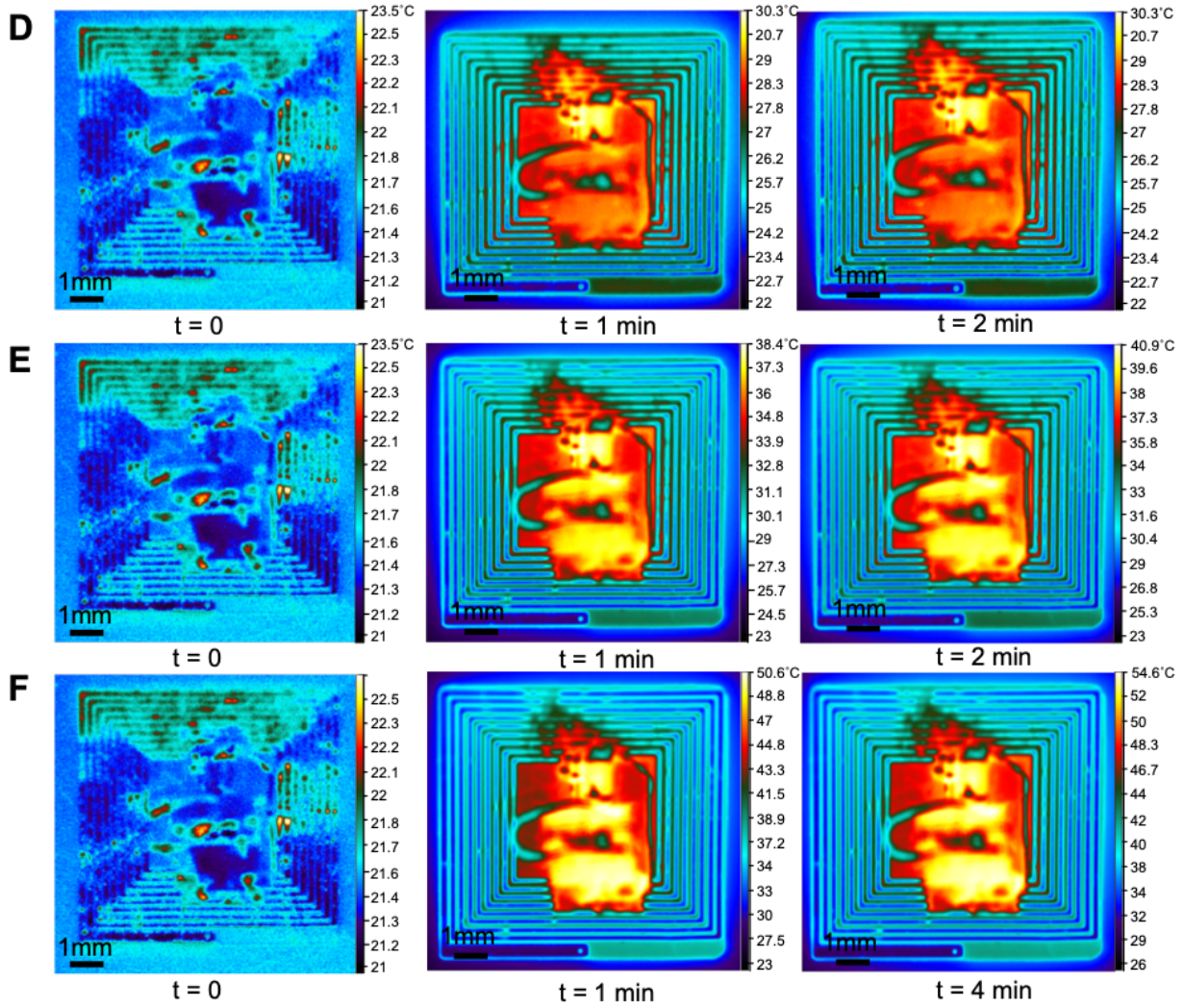

Fig. S32. Thermal analysis of the devices. (**A**, **B**, and **C**) Thermal images of a 810-nm device during the wireless powering cycle at three different power levels of -9, -6, and -3 dBm, respectively. Highest temperatures were observed at the LED metal pads and wires carrying current at the center of the device, as well as the areas in close vicinity of the LEDs. Maximum temperatures measured in these areas at low (-9 dBm), medium (-6 dBm), and high (-3 dBm) power levels were 28.8, 29.5, and 31°C. (**D**, **E**, and **F**) Thermal images of a 940-nm device running at power levels of -10, -7, and -4 dBm. Maximum temperatures observed at low, medium and high power levels were 30.3, 40.9, and 54.6 °C. Measurement setup is shown in Supplementary Fig. 31. The device was placed at the center of the TX coil (h = 0) and thermal images were recorded until no more heating was observed at the device. Even though some small areas on the device (~ 4-25 mm^2) were warmer compared to the rest of the device, quantitative analysis of the temperature over the entire surface of the device, showed that the average temperature of the device remained low. Note that these measurements were performed when the devices were positioned at h=0 cm for highest signal transfer efficiency to result in maximum temperature increase in the device for safety evaluations. The real temperature of the device during the *in vivo* experiments was significantly lower at higher heights (*i.e.*, h=1-5 cm) where the top surface of the mouse head was located most of the times during the photothermal therapy sessions (see *in vivo* thermal image in Supplementary Fig. 34). Temperature scale bars are shown on the right-side of each image.

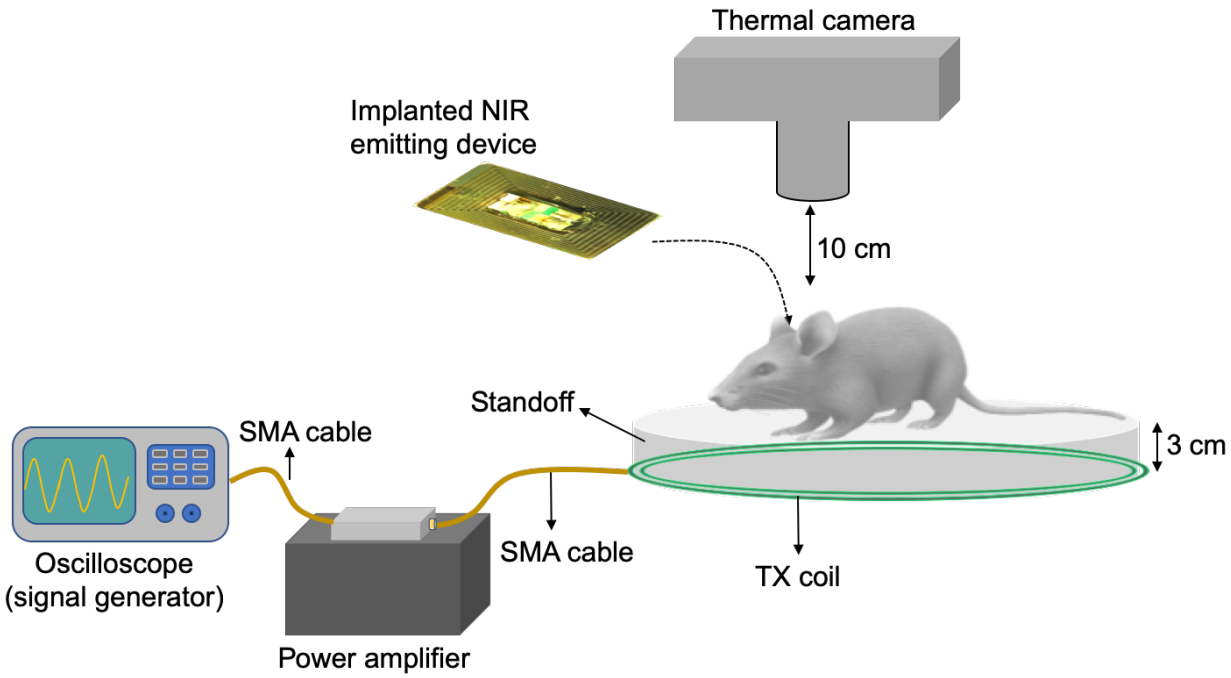

Fig. S33. *In vivo* thermal imaging setup. Schematic showing the approach used to evaluate heating profile of the implanted devices (Supplementary Fig. 34). The anesthetized mouse was placed at a distance of ~3 cm on top of the transmitter coil (TX), and thermal camera was fixed at a distance of ~10 cm above the mouse head. Since the mouse was anesthetized (head at resting position on the plastic standoff), 3 cm height was added to simulate the real position of the device in a freely-behaving mouse.

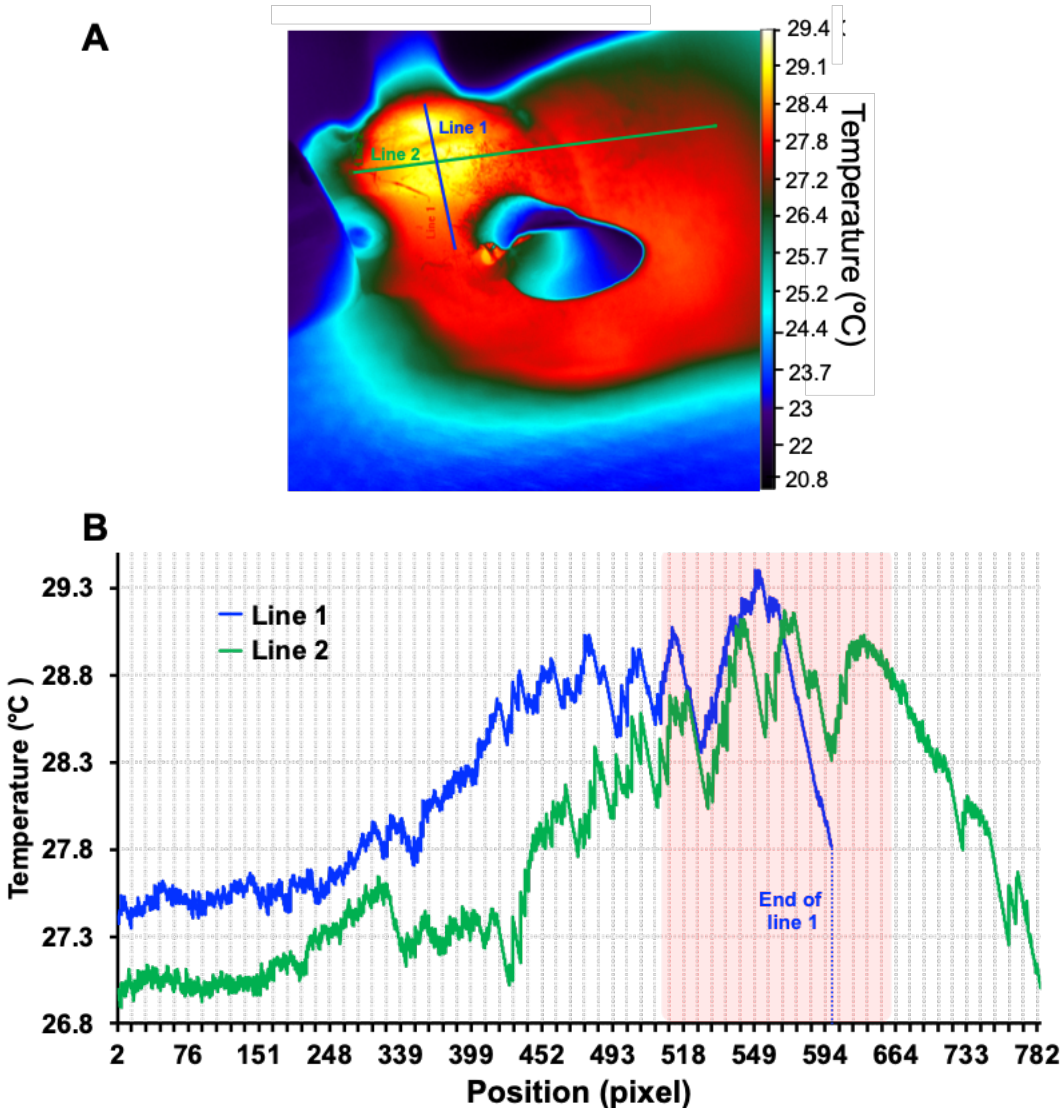

Fig. S34. Thermal analysis of the implanted devices. (**A**) Thermal image of an anesthetized mouse, 2 min after turning the implanted 940-nm device on. Medium power level (-7 dBm) was used for wireless powering of this device. (**B**) Temperature profiles along lines 1 and 2 shown in (A). Shaded area shows temperature variations around the implanted device. Imaging setup is shown in Supplementary Fig. 33.

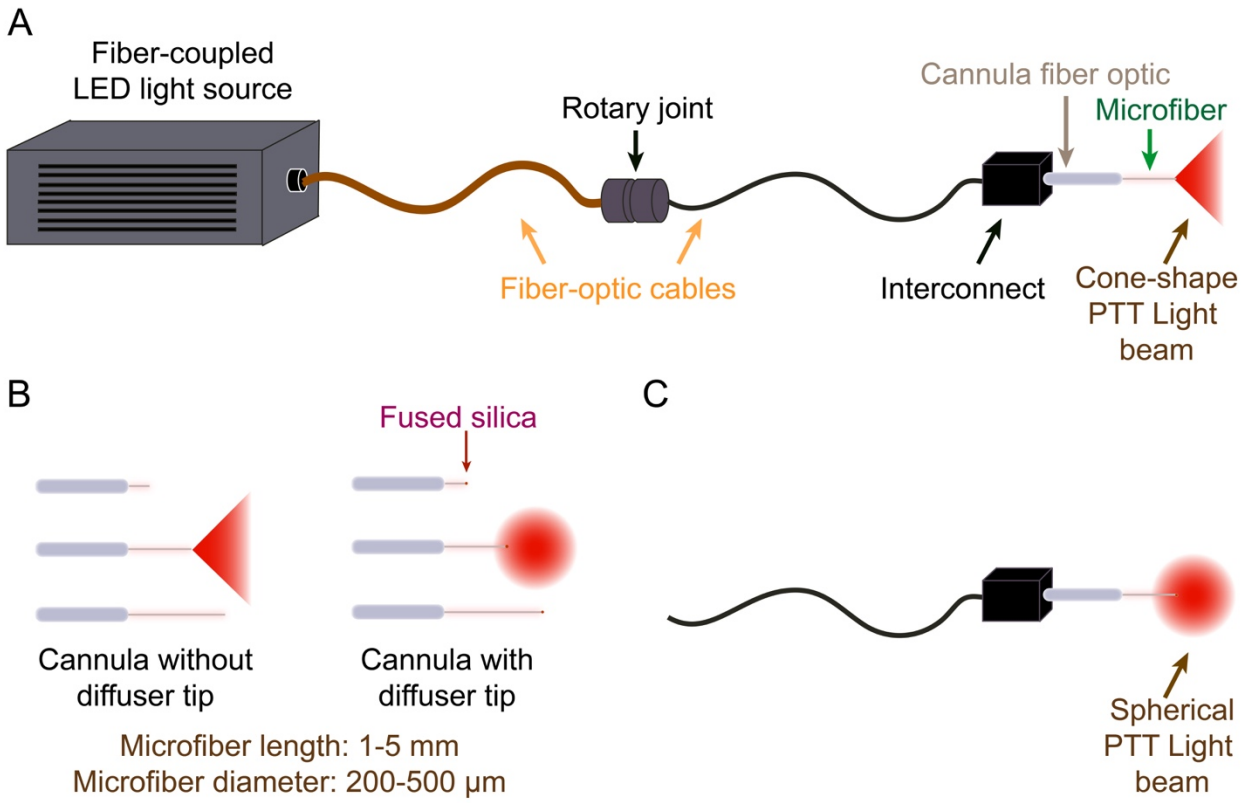

Fig. S35. Tethered light-delivery setup for photothermal therapy of the brain tumors in freely-behaving mice. (**A**) NIR light source and fiber-optic cables for delivering the light to the microfibers. These microfibers (length ~ 1-5 mm and diameter ~ 200 μm) were implanted in the brain to deliver the photothermal therapy (PTT) light to tumors in awake mice (also see Supplementary Fig. 36). (**B** and **C**) Different types of microfibers can be used for delivering cone-shape and spherical beams to tumors in different locations of the brain.

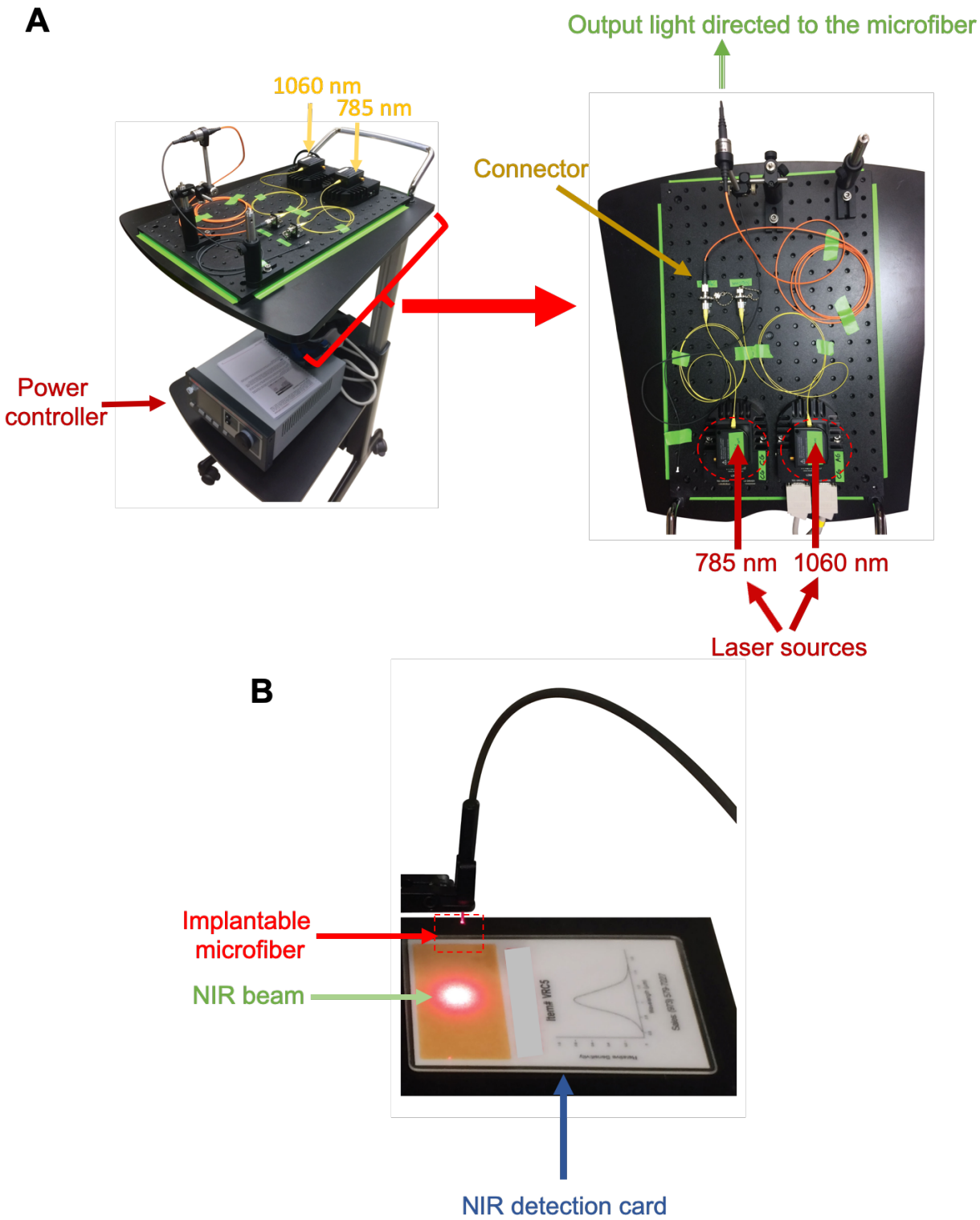

Fig. S36. Photographs showing an overview of the setup used for tethered photothermal therapy in freely-behaving mice. (**A**) NIR light sources to generate 785 and 1060 nm beams. (**B**) NIR beam detected by an IR reader card (also see Supplementary Fig. 35 for details about the implantable microfibers).

Fig. S37. Tumor implanted microfibers. Photograph showing a mouse with a microfiber implanted in the brain for NIR delivery to the tumor. Fiber-optic cables showed in Supplementary Figs. 35-36 were connected to the cannula on the mouse head for delivering light, while the mouse could freely do normal activities during the treatment.

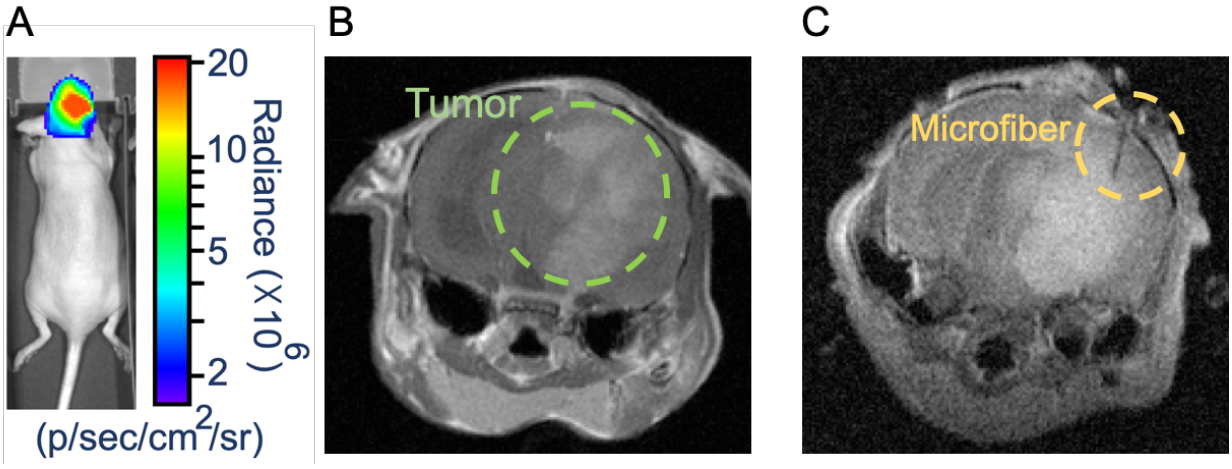

Fig. S38. Implanting the microfibers in brain tumors. (**A**) Bioluminescent imaging was used to estimate the tumor size based on bioluminescent signal intensity. (**B** and **C**) MRI was used to measure the tumor volume and determine the exact location and shape of the tumor for accurate implantation (*i.e.*, location and angle) of the microfibers. See the photograph of an implanted mouse in Supplementary Fig. 37.

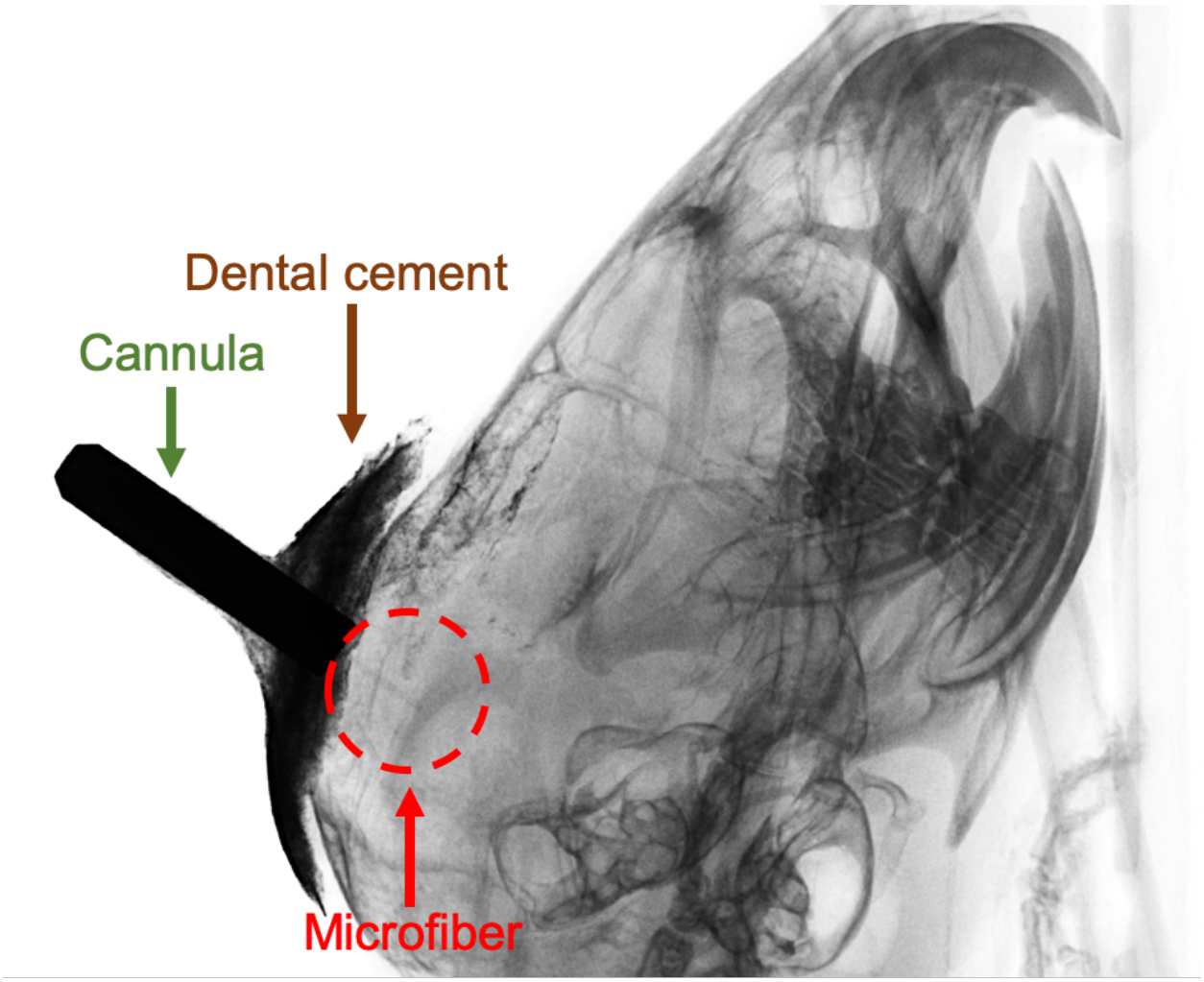

Fig. S39. X-ray image of a mouse head showing an implanted microfiber. The microfiber was guided to the tumor, based on preliminary tumor assessments using MRI results. During the photothermal therapy sessions, cannula was connected to fiber-optic cables for delivering NIR light to the microfiber. The implanted device was fixed on the mouse brain using dental cement.

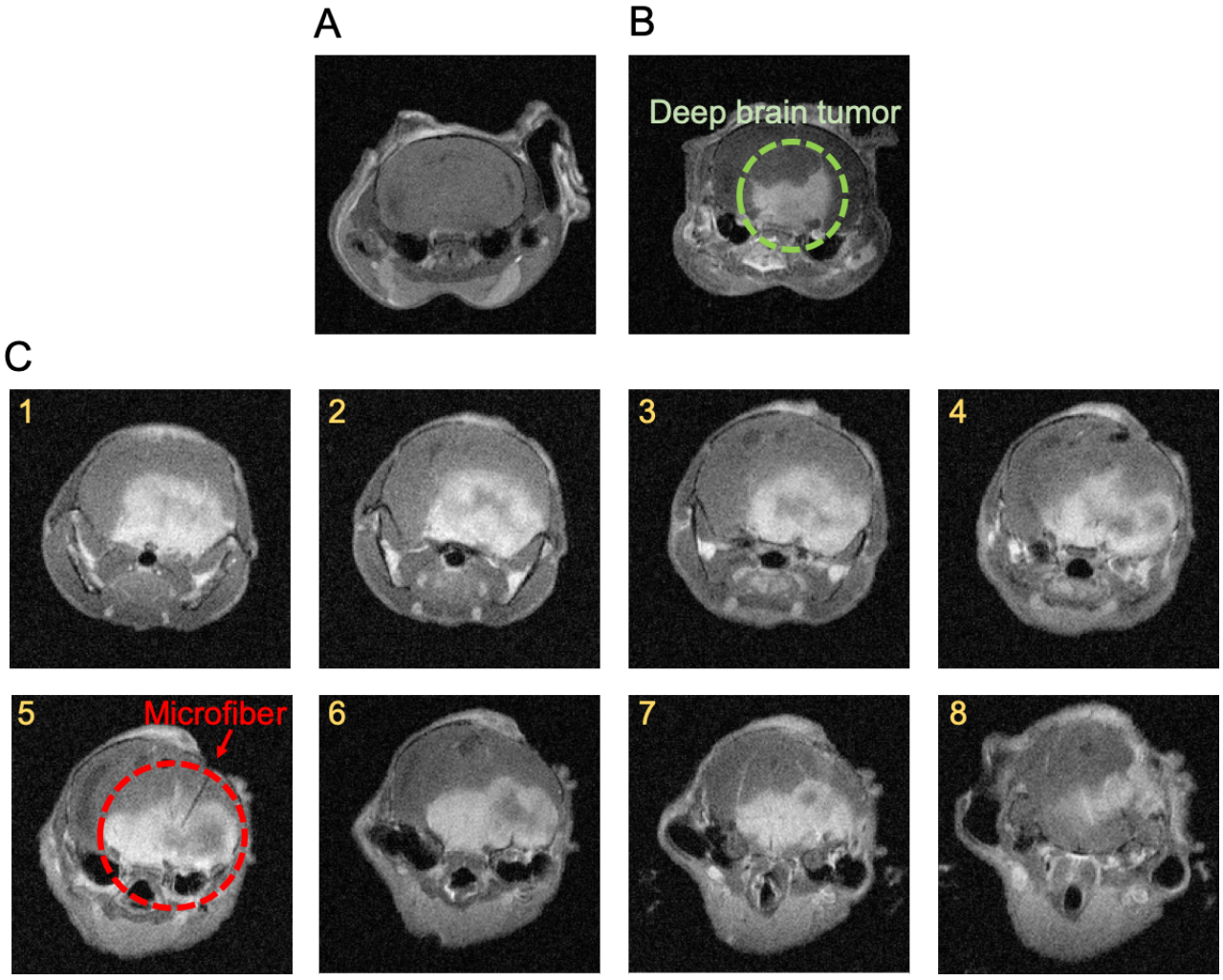

Fig. S40. Versatility of the fiber-optic approach for photothermal therapy of the deep brain tumors in freely-behaving mice. (**A** and **B**) T1-MRI before and after intraperitoneal injection of the Gd-contrast agent, showing a tumor in deeper regions of the brain. (**C**) T1-MRI of consecutive brain slices (1-mm thick) showing a tumor-implanted microfiber and tumor necrosis (darker zone around the fiber tip) as the result of photothermal therapy.

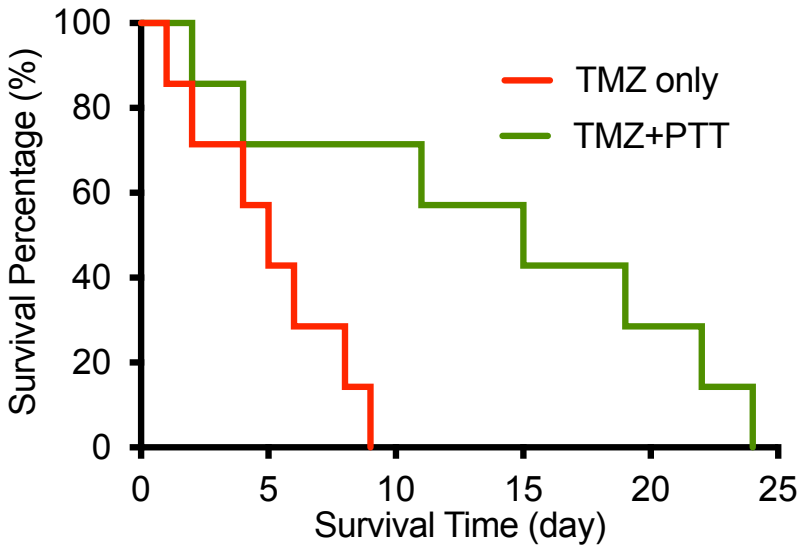

Fig. S41. Combination therapy. Survival of the mice with U87 tumors treated with simultaneous wireless photothermal therapy (PTT) and chemotherapy (temozolomide or TMZ). Significant difference was observed when comparing these two treatment groups ($p = 0.0157$, using the log-rank test, n=7/group, total=14)

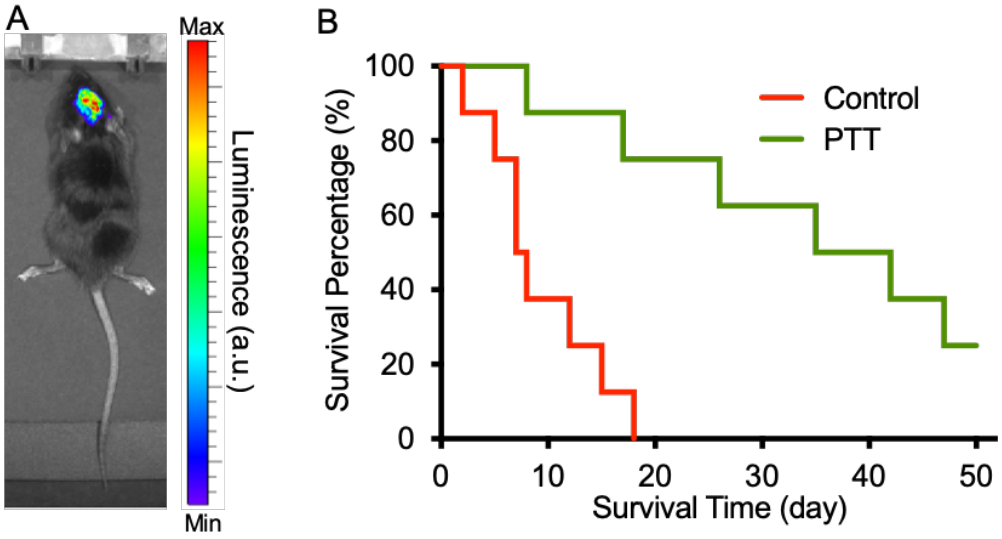

Fig. S42. Wireless photothermal therapy in immunocompetent mice. (A) BLI image of a representative immunocompetent C57BL/6J mouse with orthotopic syngeneic GL26 tumor. (B) Survival graph of the immunocompetent mice with orthotopic GL26 tumors treated with wireless photothermal therapy (PTT) in comparison with control mice with the same tumor [NPs (-), Implantation (-)]. Significant difference was observed when comparing these two treatment groups ($p = 0.0008$, using the log-rank test, n=8/group, total=16)

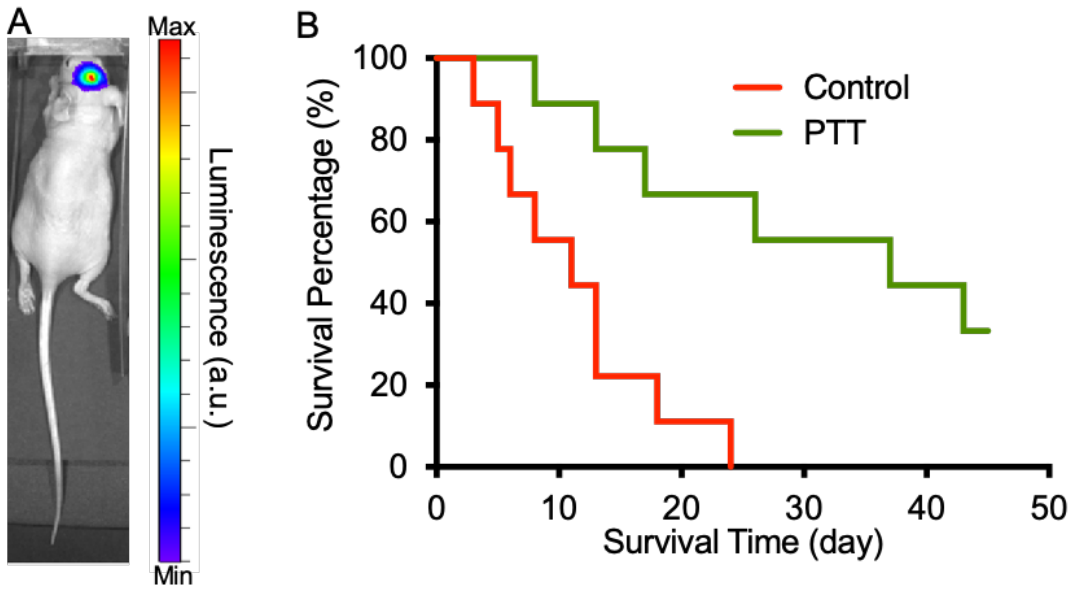

Fig. S43. Evaluating wireless photothermal therapy in human-derived GBM39 tumors. (A) BLI image of a representative mouse with orthotopic GBM39 tumor. (B) Survival pattern of the mice with GBM39 tumors with and without wireless photothermal therapy (PTT *vs.* control, p = 0.0022, using the log-rank test, n=9/group, total=18)

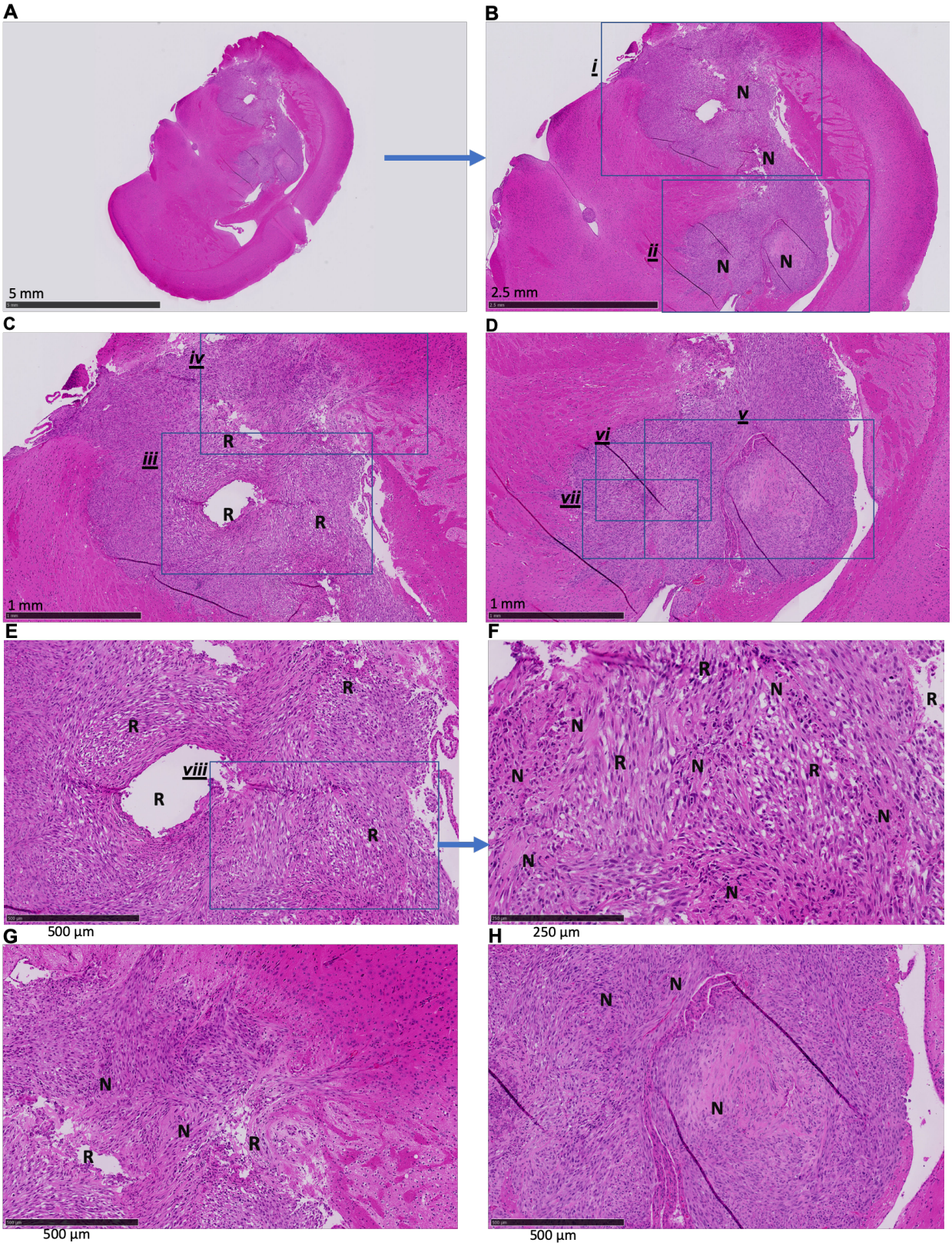

Fig. S44. Histological analysis of the U87 brain tumors after wireless photothermal treatment. Hematoxylin and eosin (H & E) stained brain tumor sections were analyzed using

bright-field microscopy. Images in B-H show zoomed areas in different locations of the tumor (medially located darker purple region) in the coronal whole brain section shown in (A). (C) and (D) show magnified images of the zones *(i)* and *(ii)* in part (B), respectively. (E) and (G) show magnified images of the zones *(iii)* and *(iv)* in image (C). (F) is the magnified image of the zone *(vii)* in (E). (H) is the magnified image of the zone *(v)* in (D). Some selected and representative areas that show necrosis and dead cells (shown with "N") or responded to our treatment (shown with "R", *e.g.*, areas that appear to be tumor shrinkage in response to thermal effects) are marked in different images and verify photothermal treatment effects on the tumor. Dead cells were distinguished as darker sharp points through the sections mostly adjacent to necrotic regions. These features were not observed in tissue sections obtained from control U87 mice without any treatment (n=5 brains, see Supplementary Fig. 45, control U87).

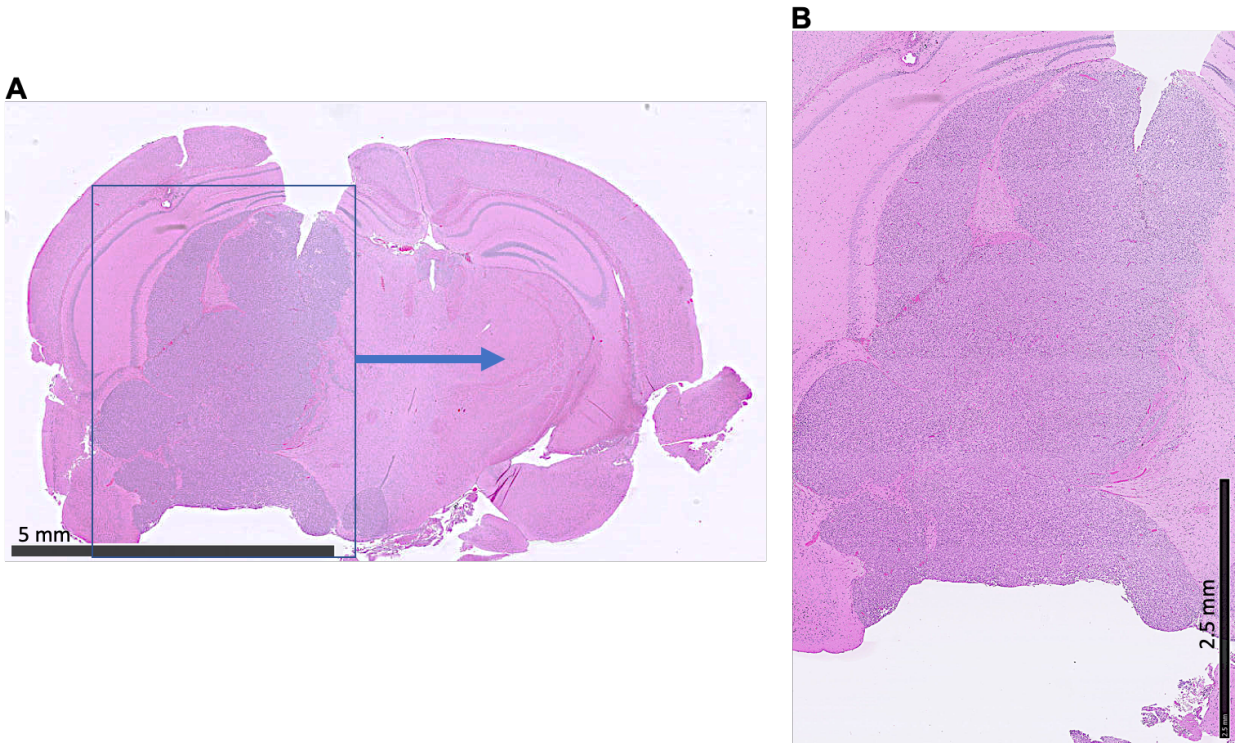

Fig. S45. Histological analysis of the U87 brain tumors without any treatment (control). Hematoxylin and eosin **(**H & E) stained tissue sections were analyzed to be compared with treated tumors (Supplementary Fig. 44). Compared to treated mice, the tumors grew larger in untreated mice. In addition, the untreated tumors were lacking areas of response and necrosis ("R" and "N" shown in Supplementary Fig. 44) and were densely composed of cancer cells due to unchecked proliferation (n=5 brains). B is a zoomed in version of A.

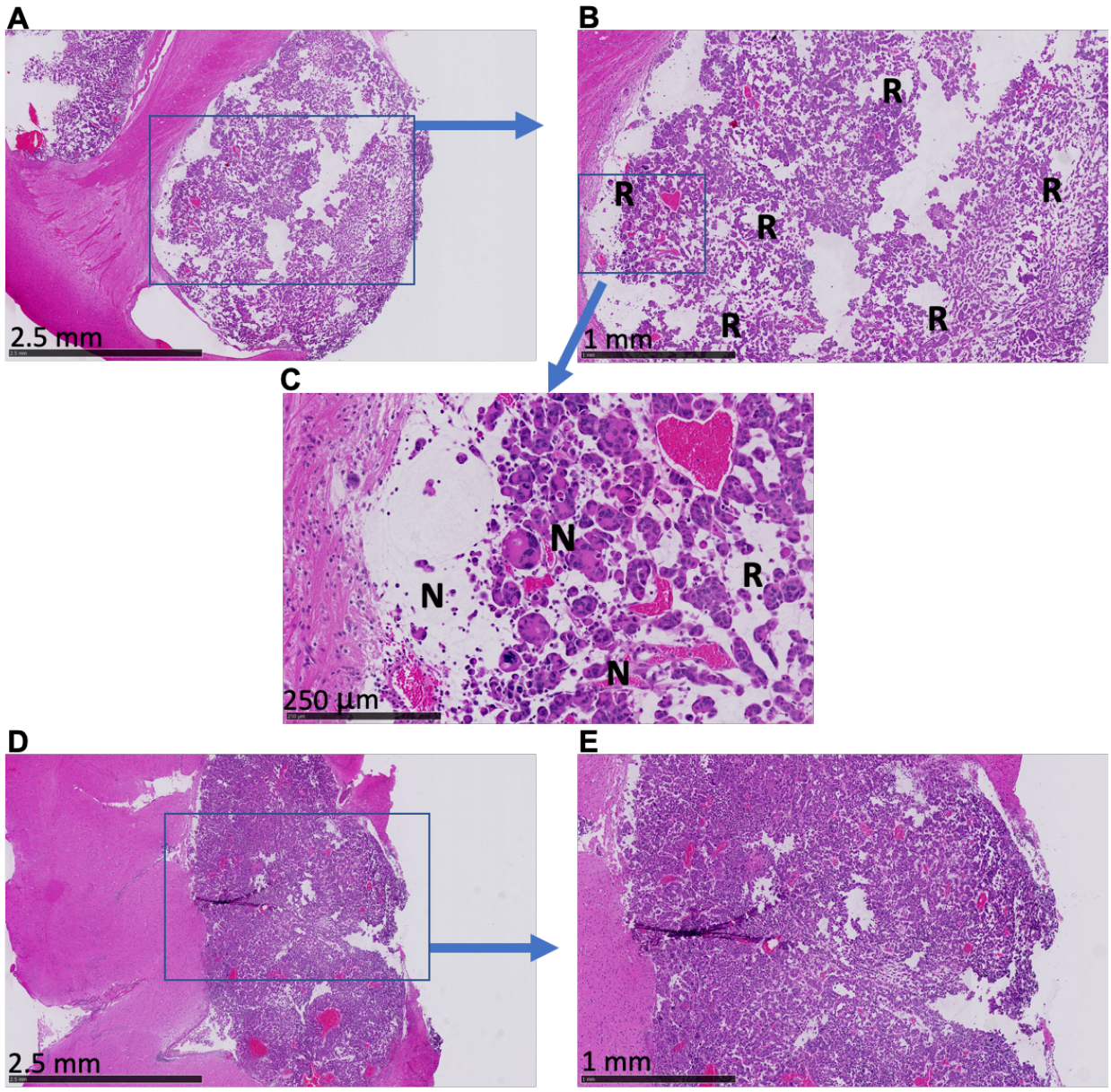

Fig. S46. Histological analysis of the GL26 brain tumors (immunocompetent syngeneic model) with and without wireless photothermal treatment. (A-C) Hematoxylin and eosin (H & E) stained tissue sections from the immunocompetent mice with syngeneic GL26 tumors after photothermal treatment. Necrosis and dead cells (sharp dark dots) are marked with "N", and tumor areas that responded to treatment (*i.e.*, shrinkage and lower number of tumor cells and significantly perturbed tumor tissue structure) are marked with "R". Both features were observed in different regions of the photothermally treated tumors and some representatives are shown in these images (n=5 brains). (D) and (E) show histological images of a control GL26 mouse without any treatment. The untreated tumors were lacking areas of response ("R") or necrosis similar to the treated brains and were densely composed of cancer cells due to unimpeded proliferation (n=5 brains).

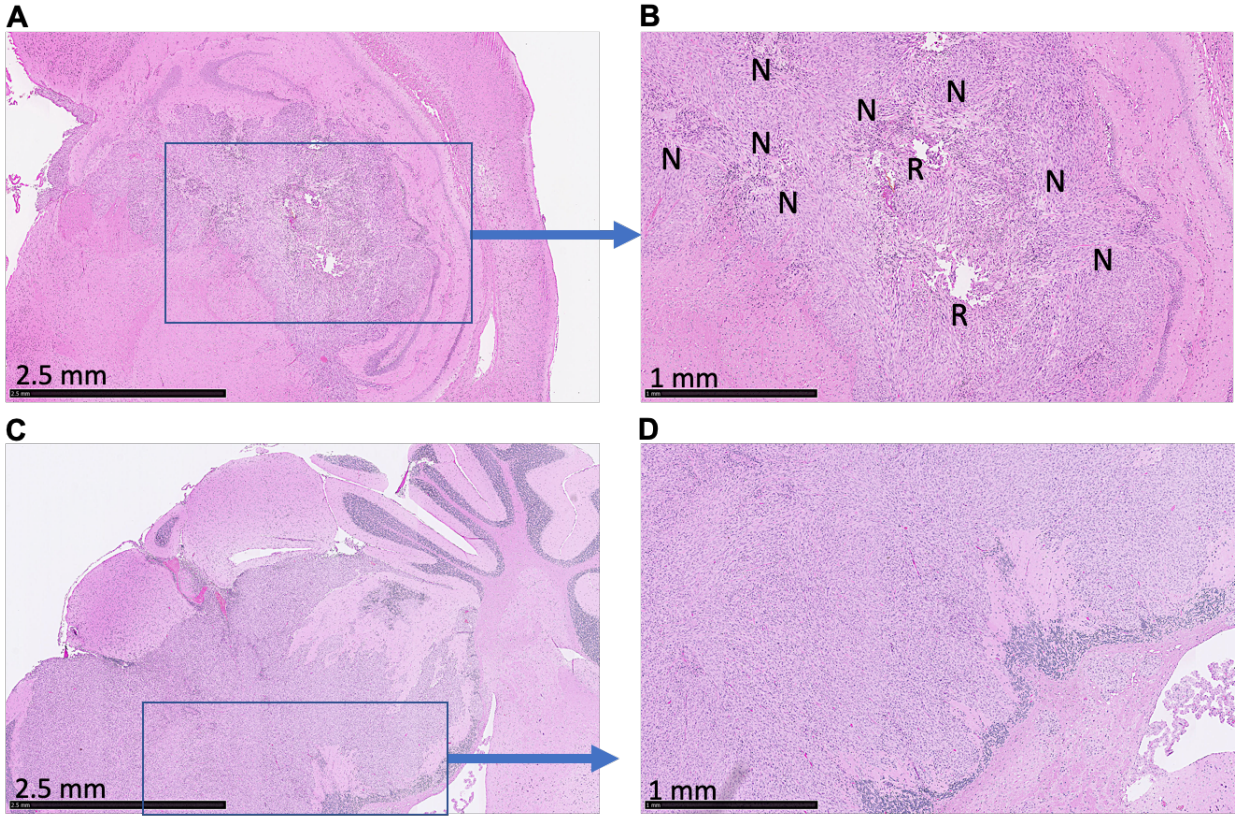

Fig. S47. Histological analysis of the GBM39 brain tumors (immunodeficient xenograft model) with and without wireless photothermal treatment. (A-B) Hematoxylin and eosin (H & E) stained tumor tissues after treatment compared with control tumor tissues without any treatment (C-D). Necrosis and dead cells are marked with "N". Also, tumor areas that responded to our treatment (*i.e.*, shrinkage and a generally perturbed tissue structure) are marked with "R" and both features were consistently observed in treated tumors, compared with uniform and denser distribution of the tumor cells in control tumors (n=5 brains). Note the larger tumor mass in the untreated brain compared to the treated brain. In addition, the untreated tumors were lacking areas of response ("R") or necrosis ("N") similar to treated brains and were densely composed of cancer cells due to unimpeded proliferation.

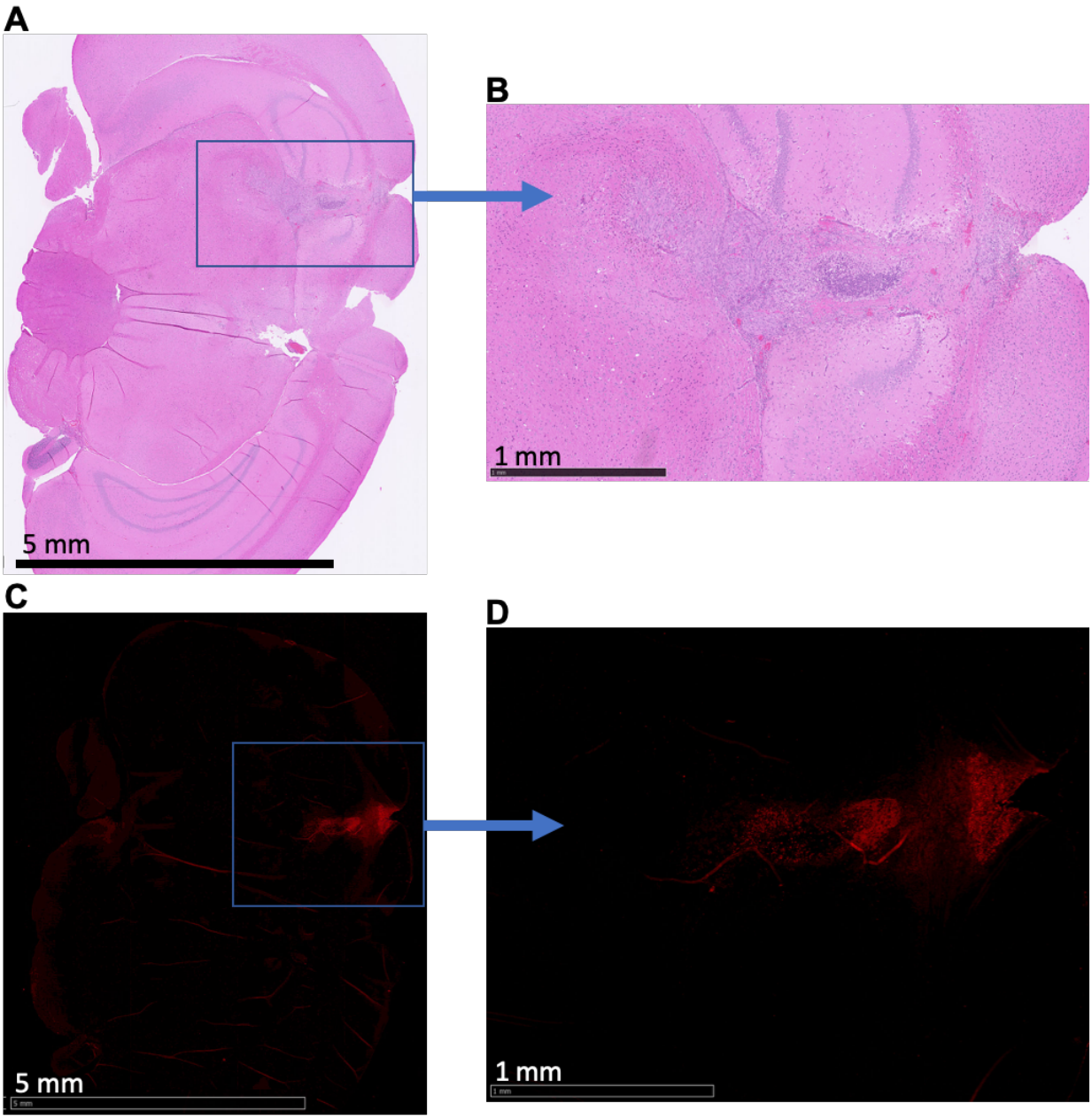

Fig. S48. Tumor cells apoptosis as a result of short-term wireless photothermal treatment. (A-B) H & E stained image of an early stage orthotopically implanted GBM39 tumor (7-day post-implantation) showing apoptosis after a single-session wireless photothermal therapy (1 day treatment). (C-D) Fluorescent images of the same tissue after TUNEL staining. Red spots verify early apoptosis after a single day treatment.